# UNIVERSIDAD AUTÓNOMA DE NUEVO LEÓN

## FACULTAD DE CIENCIAS FÍSICO MATEMÁTICAS


TESIS

# A MATHEMATICAL MODEL FOR THE PREDICTION OF THE SCALE LAYER FORMATION ON ASTM A510/A853 COLD-DRAWN HYPOEUTECTOID STEEL WIRE AFTER BATCH ANNEALING

POR

JOSÉ ALFREDO SÁNCHEZ DE LEÓN

SOMETIDA PARA OBTENER EL GRADO DE

MAESTRÍA EN CIENCIAS CON ORIENTACIÓN EN MATEMÁTICAS

SEPTIEMBRE 2021

# UNIVERSIDAD AUTÓNOMA DE NUEVO LEÓN

## FACULTAD DE CIENCIAS FÍSICO MATEMÁTICAS

## CENTRO DE INVESTIGACIÓN EN CIENCIAS FÍSICO MATEMÁTICAS



TESIS

# A MATHEMATICAL MODEL FOR THE PREDICTION OF THE SCALE LAYER FORMATION ON ASTM A510/A853 COLD-DRAWN HYPOEUTECTOID STEEL WIRE AFTER BATCH ANNEALING

POR


JOSÉ ALFREDO SÁNCHEZ DE LEÓN


SOMETIDA PARA OBTENER EL GRADO DE

MAESTRÍA EN CIENCIAS CON ORIENTACIÓN EN MATEMÁTICAS


SAN NICOLÁS DE LOS GARZA, N. L. SEPTIEMBRE 2021

# UNIVERSIDAD AUTÓNOMA DE NUEVO LEÓN

## FACULTAD DE CIENCIAS FÍSICO MATEMÁTICAS

## CENTRO DE INVESTIGACIÓN EN CIENCIAS FÍSICO MATEMÁTICAS

Los miembros del comité de tesis de la subdirección de posgrado de la Facultad de Ciencias Físico Matemáticas, recomendamos que la tesis "A Mathematical Model for the Prediction of the Scale Layer Formation on ASTM A510/A853 Cold-Drawn Hypoeutectoid Steel Wire After Batch Annealing", realizada por el **Ing. José Alfredo Sánchez de León**, con número de matrícula 0975988, sea aceptada para su defensa para opción al grado de Maestría en Ciencias con Orientación en Matemáticas.

El Comité de Tesis

**Dra. Lilia Alanís López**
Asesor

**Dra. María Luisa Daza Torres**
Co-Asesor

**Dr. Alfredo Alanís Durán**
Sinodal

Vo. Bo.

**Dr. Omar Jorge Ibarra Rojas**
Coordinador del Posgrado en Ciencias con Orientación en Matemáticas

SAN NICOLÁS DE LOS GARZA, N. L. SEPTIEMBRE 2021

Dedicado a mi mamá:
Mary

We must know, we shall know.

– David Hilbert

# ABSTRACT

A Mathematical Model for the Prediction of the
Scale Layer Formation on ASTM A510/A853 Cold-Drawn
Hypoeutectoid Steel Wire After Batch Annealing
by
José Alfredo Sánchez de León
Maestría en Ciencias con Orientación en Matemáticas
Universidad Autónoma de Nuevo León, 2021

Annealed hypoeutectoid ASTM A510/A853 [8], [9] steel wire is widely used in the construction industry due to its mechanical properties, which makes it a very versatile material to work with. This work concerns the prediction of the thickness of the scale layer of the AISI/SAE [54] hypoeutectoid steel wire once subjected to a batch annealing process. We propose a mathematical model to approach oxidation, which befalls during the process. The model treats this phenomenon as a non-isothermal instance; it takes as input a heating curve, a cooling curve, and a holding time that corresponds to the heating and cooling cycles and a heating holding cycle. We assume the temperature of material outer spiral segments as the furnace atmosphere temperature. With the aid of these models, it is possible to predict the oxide scale layer of the outer spirals segments of the annealed drawn wire coils after batch annealing with reasonable accuracy. We did not find visible evidence of decarburization; the steels of the study in this work do not decarburize [41]. As an approximation, we assumed that the temperature of the outside of the drawn wire coils equals the furnace atmosphere.

El alambre ASTM A510/A853 [8], [9], de acero hipoeutectoide recocido es un producto que es ampliamente utilizado hoy en día en la industria de la construcción debido a sus propiedades mecánicas, las cuales lo hacen un material muy versátil para trabajar. Este trabajo aborda la predicción del espesor de la capa de óxido o cascarilla del alambre de acero hipoeutectoide AISI/SAE [54] una vez que es sujeto al tratamiento térmico de recocido batch. Un modelo matemático ha sido propuesto para llevar a cabo esta tarea. El modelo aborda el fenómeno como una instancia no-isotérmica, toma como parámetros las curvas de calentamiento, de enfriamiento y tiempo de sostenimiento, que normalmente tienen lugar en el proceso industrial. Con la ayuda de este modelo puede ser posible predecir el espesor de capa de cascarilla formada en las espirales externas del alambre recocido con buena exactitud. No se encontró evidencia de decarburización en el material; el acero que es objeto de estudio en este trabajo, no decarburiza de hecho [41]. Hemos asumido, como aproximación, que la temperatura de las espirales externas de las bobinas de alambre poseen la temperatura de la atmósfera del horno.

# TABLE OF CONTENTS

PAGE

# AGRADECIMIENTOS

Primeramente quiero agradecer a mi mamá María del Rosario de León Rodríguez, por todo su apoyo brindado y comprensión durante el tiempo que he estado estudiando el posgrado y realizando este trabajo, y por todo su amor durante toda mi vida. Quiero agradecer al Ing. Eloy Cavazos Galindo por su constante apoyo, su liderazgo y consejo durante todo este tiempo que he estado laborando en Planta Trefilados, y por darme la oportunidad de estudiar este posgrado para seguir preparándome y superándome como persona. Agradezco a Grupo Villacero por todo el apoyo brindado para la realización de mis estudios de posgrado y el desarrollo de este trabajo, por permitirnos utilizar sus instalaciones para la realización de las pruebas experimentales, y la posibilidad de efectuar la publicación de los resultados obtenidos. Agradezco al Dr. Francisco Javier Almaguer y al comité del CICFIM por su recibimiento en esta institución y por brindarme la oportunidad de llevar a cabo mis estudios paralelamente con mis actividades laborales. Quiero dar las gracias a mis asesoras de tesis, la Dra. Lilia Alanís López y a la Dra. María Luisa Daza Torres, por su apoyo, comprensión y guía para el desarollo de este trabajo. Finalmente me gustaría agradecer a la Dra. Alexandra Elbakyan por la creación del proyecto Sci-Hub, el cuál coadyuvó en gran medida en la realización de este trabajo.

Muchas gracias a todos ustedes.

# CHAPTER 1
# INTRODUCTION

A wire is a single cylindrical solid body with many applications, including electrical wiring, cable manufacturing, tension-loaded structural components, springs, paper clips, spokes for wheels, and stringed musical instruments. Drawing is a metalworking process that uses tensile forces to stretch metal; it is employed to reduce the cross-section of a wire by pulling the wire through a single or series of drawing die(s), usually performed at room temperature. The output from this process is known as drawn wire or cold-drawn wire. During ASTM A510/A853 [8], [9] wire drawing production processes, microscopic shifting takes place inside the material structure. Steel grain enlarges axially; this shows up as essential changes in its macroscopic properties, mainly because tensile stress increments drastically. Recovering the microstructure and turning the material workable again is desirable; that is why the material is submitted to a heat treatment process known as annealing. In this process [32], the steel wire overheats, usually up to around 700 - 900°C. In the interim, the distorted cold-worked lattice structure [57] is changed back to one that is strain-free; this is carried out entirely in the solid-state and is usually followed by slow cooling in the furnace [56]. The final product is known as annealed wire. There is a continuous annealing process in which the steel wire continuously receives heat individually [22], and batch annealing setups, where steel wire coils are placed together into a furnace overheated generally between 3 to 8 hours, see Figure 1.1.

Oxidation is a chemical reaction that takes place during this process [61], and it is what generates the scale on the surface of the finished product. This work raises a mathematical model that predicts the thickness of the scale layer formation on the wire surface after the annealing process. Firstly the isothermal case is addressed; next, it extends to the non-isothermal instance in a batch setup. We conducted several experimental tests; through this model, we predicted the scale formation over the outer spirals of the annealed wire coil with reasonably good accuracy.

## 1.1 Aims and Scope

This work aims to study the oxidation phenomenon on the surface of the annealed hypoeutectoid (low carbon) steel wire during the batch annealing process. The first specific aim is to develop a mathematical model from which it can be possible to predict

**Figure 1.1.** Visualization of typical facility setup for batch annealing process of steel cold-drawn wire.

the thickness of the scale lawyer formation of the outer spirals of wire coils subjected to the atmosphere of a bell-type furnace. The second specific aim is to use the here-raised model as a measuring tool to be used together with the industrial quality control lab tests to determine this critical variable value in the annealing process. To reach these aims, we approach oxidation as an isothermal case (Section 4.1). We took from [67] the constant parameters they obtained, to use them in our model. Using the proposed perspective, we extend this scheme to the non-isothermal case through a mathematical transformation [53]. Since this phenomenon is thermally activated, temperature is a critical variable. We will see later in Section 4.1 that the isothermal oxidation model's input is a constant temperature value, but this would be useless in our process. The

idea to extend the model to the non-isothermal case comes from the necessity to enable the model to employ the furnace heating and cooling curves as input parameters.

Finally, to evaluate the model's accuracy (Section 5.1), the computed values from the model are validated against the experimental data obtained from samples in a series of tests conducted in an industrial annealing setup.

## 1.2 Context

As stated above, to perform the drawn wire's annealing, there exist two types of process: batch annealing and continuous annealing. This last one is increasingly being employed mainly due to some advantages over the former, like higher production rates and more homogeneous properties on the finished product that can be obtained. Therefore, the recent research endeavors are focused on the continuous process. However, batch annealing is a heat treatment process that is still widely used, mainly in Latin America.

## 1.3 Motivation

Oxide-scale layer is a critical product property that quality control measures at process completion. It is so important that depending on its final use, some markets do not buy the annealed drawn wire if it does not have enough oxide-scale layer on its surface. On this point, it could be desirable to rely on a mathematical model to predict the thickness of the oxide-scale layer in terms of the process control variables and steel coil properties.

At least at the time of this writing, we could not find a model in the existing literature that described the drawn wire oxide surface formation in the batch annealing process; thus developing a mathematical model to address it is very worthwhile.

## 1.4 Content

This document consists of five chapters. The first chapter serves as an introduction to the main problem studied in this work. It unfolds the general background and a brief introduction to the process; it exposes why this subject is essential to be studied. There are defined aims and details about how this project was approached, and lastly, the methodology that drove this endeavor.

Chapter two explains what hypoeutectoid steel is to better understand the materials used in the experimental tests performed in this work. It describes the manufacturing standards that rule the annealed drawn wire production and the performed tests. This aspect connects with Chapter 4 since the obtained results from the model raised there

validate against experimental data on the basis exposed here.

Chapter three presents the needed theoretical background to raise the mathematical model. It settles the mathematical tools that we employ. It also offers a description of the Arrhenius equation, the chemical reactions implicated in the steel oxidation phenomena, and an explanation of the heat transfer process. This chapter links to Chapter 4 because all the thermodynamics and chemistry exposed here constitute the mechanism that underpins the oxidation phenomenon.

Chapter four extends prior results to the isothermal case. In this chapter, we approach the primary goal of this work: developing a mathematical model that describes the oxide-scale layer growth in terms of the process heating and cooling curves. The arising results are validated in Chapter 5.

Chapter five presents the results of the performed annealing tests. It exposed the scale thickness values obtained through the metallographic tests. Afterward, we compare the computed values obtained from the mathematical model against the experimental data set. This chapter, altogether with Chapter 4, represents the main results obtained in this thesis.

Chapter six states the conclusions obtained from the development of this work and proposes possible further research.

In this thesis were also included three appendices that help to understand several ideas and the content of this thesis.

## 1.5 Methodology

We performed the following steps as part of the implemented methodology:

1. Literature review on topics about metalworking process, heat treatments, steel properties, and steel oxidation.
2. Literature review on specific mathematical models concerning oxidation phenomenon and heat transfer.
3. Survey on Bell-type furnace design, features, and operation, with the aid of the maintenance department (at work) and furnace manufacturer.
4. Chemical analysis of combustion emission gases from the employed annealing furnace on the experimental tests.

5. Rise a mathematical model that describes the oxide-scale layer growth on steel wire coils during the annealing process regarding the process variables and material properties.
6. Set the required experimental annealing tests and other technical details required in this work (machinery, materials, operational conditions).
7. Request authorization at work to perform the corresponding experimental tests on the production annealing furnace and plant facilities.
8. Compute the scale layer values utilizing the mathematical model raised in this document regarding its input variables.
9. Metallographic examination on the experimentally worked samples from the annealing tests to measure the resulting scale size.
10. Perform a comparison of the experimentally measured data against the model output values.

# CHAPTER 2
# MATERIALS, PROCESS AND TESTS

This section reveals the basic concepts regarding the material that we describe in our mathematical model. On this basis, it introduces the idea of hypoeutectoid steel and some of its inherent properties as a crystalline material. One mechanical property inherent to the material in the study is tensile strength. This term briefly describes the wire-drawing process and the annealing process and the main aspects of this process we approach in this model. Finally, it presents the metallography test and some intuitive examples to understand its importance regarding the validation of the model, which connects with Chapter 5.

## 2.1 Elements and Some Properties

Before delving into hypoeutectoid steel as a material, it is worth describing the essential components that make it up. This section describes the chemical elements that constitute the steel as an alloy and also reveals allotropy, a property that plays a vital role in some of its properties.

Before we review the chemical elements, we will examine the definition of element. An element can be defined as a pure substance that is made up of atoms of the same type and cannot be split into single components by normal physical-chemical operations. Elements are the basis that builds all matter. Next, we describe the most common elements found in steels.

[34] states the following.

"*Iron*. It is a metallic element with the symbol Fe [20] (from the Latin: Ferrum) and atomic number 26. Is a grayish metal, which until recently was never used pure. It melts at 1525°C and boils at 2450°C. All commercial irons contain perceptible quantities of carbon, which affect their properties. Iron combined with carbon is termed steel. It oxidizes easily and is also attacked by many acids. Besides being the major constituent for all steels, iron is the base metal for numerous iron alloys.

*Manganese.* A metallic element, symbol Mn, and atomic number 25; has a silvery-white color with purplish shades. It is brittle but hard enough to scratch glass; has a melting point of 1245°C and a boiling point of 2061°C. It decomposes in water slowly; it is not used alone as a construction metal. Steels usually contain at least 0.3% manganese, which acts in a three-fold manner: it assists in deoxidation of the steel, prevents the formation of iron sulfide inclusions, and promotes greater strength by increasing the hardenability of the steel; nearly all steel now contains manganese.

*Silicon.* A metallic element, symbol Si, and atomic number 14, of crystalline appearance, solid at room temperature. Has a melting point of 1434°C and a boiling point of 3265°C. Usually, only small amounts (around 0.2%) are present in steel when silicon is used as a deoxidizer. Silicon dissolves in iron and tends to strengthen it. Weld metal usually contains approximately 0.5% silicon as a deoxidizer. Some filler metals can contain up to 1.0% to provide enhanced cleaning and deoxidation for welding on contaminated surfaces. When these filler metals are used for the welding of clean surfaces, the resulting weld metal strength will be markedly increased. The resulting decrease in ductility could present cracking problems in some situations.

*Sulphur.* A non-metallic element, symbol S, and atomic number 16; it forms a crystalline mass of a pale-yellow color, solid at room temperature. Has a melting point of 115°C and a boiling point of 444.6°C. It is usually an undesirable impurity in steel rather than an alloying element; in amounts exceeding 0.05%, it tends to cause brittleness and reduce weldability.

*Phosphorus.* A nonmetallic element, symbol P, and atomic number 15. There are two common forms of phosphorus, yellow and red. The former, also called white phosphorus, is the most common form. It has an appearance of waxy white. At room temperature it is solid; has a melting point of 44.15°C and a boiling point of 280.5°C. It is an essential element in the human body. A normal person has more than a pound of this element in the system. Phosphorus is also considered to be an undesirable impurity in steels. It is normally found in amounts up to 0.04% in most carbon steels. In hardened steels, it tends to cause embrittlement."

To better understand the above elements and their properties, we advise the reader to review [26].

There is an essential property of some elements related to the steel itself and its characteristics. This is allotropy. We will review it next.

## 2.2 Allotropy

According to how atoms or ions arrange concerning one another, researchers can classify solid materials. One kind of material is when the atoms situate in a periodic array over large atomic distances. This is a crystalline body (see Figure 2.1). In this case, after solidification, the atoms will position themselves in a constant 3D scheme, where each atom joins to the nearest atoms. The normal solidification process causes many ceramic materials, metals, and polymers to form crystalline structures. Some materials do not crystallize; in this case, the long-range atomic order is not present; these materials are termed noncrystalline, or amorphous materials; one such example is glass.

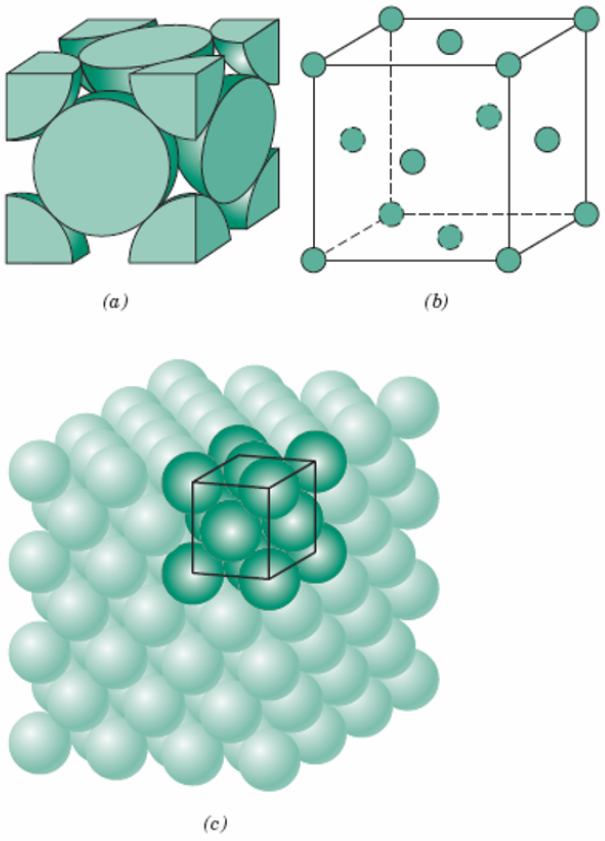


**Figure 2.1.** Crystalline structure representation [3]. (a) A hard sphere unit cell representation, (b) a reduced-sphere unit cell, and (c) aggregate of many atoms [48].

Some characteristics of crystalline bodies depend on their crystal structure; this is how atoms, ions, or molecules are placed in space. Several crystal structures exist, all having long-range atomic arrangements; these vary from the simple conformations for metals to some more complex ones.

The property of some elements (including metals and alloys) that exhibit different crystal structures at different temperatures is called allotropy [17]. Two allotropic forms of the element carbon — diamond and graphite — are dramatically dissimilar in properties and their relative value. Another example, oxygen has two allotropes: $O_2$ and $O_3$ (ozone). Allotropy is a crucial property found in many materials; allotropic changes constitute the basis for the heat treatment of many engineering materials.

The theory just discussed in this section will be constructive to understand the iron-iron carbide diagram treated in the next Section 2.3.

## 2.3 The Iron-Iron Carbide Phase Diagram

The iron-iron carbide or Fe-C phase diagram (see Figure 2.2) represents the different crystalline arrangements, or phases, of the carbon steels in a state of equilibrium state. It forms by slow cooling from the molten metal. In [34] they state:

"This is not a realistic view of the microstructural phases that exist during normal fabrication processes because the heating and cooling rates affect the temperatures at which the suggested phase transformations occur. This effect can be seen in the temperature difference between $A_1$, the equilibrium lower transformation temperature, and $Ar_1$, the lower transformation temperature upon cooling. Although not shown, there is also a lower transformation temperature upon heating, $Ac_1$, which is somewhat higher than $A_1$".

The $Ac_1$ temperatures depict the start point of the transformation between the alpha ferrite and the gamma austenite upon heating.

The phase diagram in Figure 2.2 also shows an equilibrium upper-transformation temperature $A_3$. Similar to the variations noted for $A_1$, there are also upper-transformation temperatures upon heating and cooling ($Ac_3$ and $Ar_3$, respectively). These temperatures dictate the points at which the material structure turns unstable and undergoes a transformation to a different crystalline structure. We can see that carbon steels, with a typical maximum carbon content of less than 0.35% for pressure-containing applications,

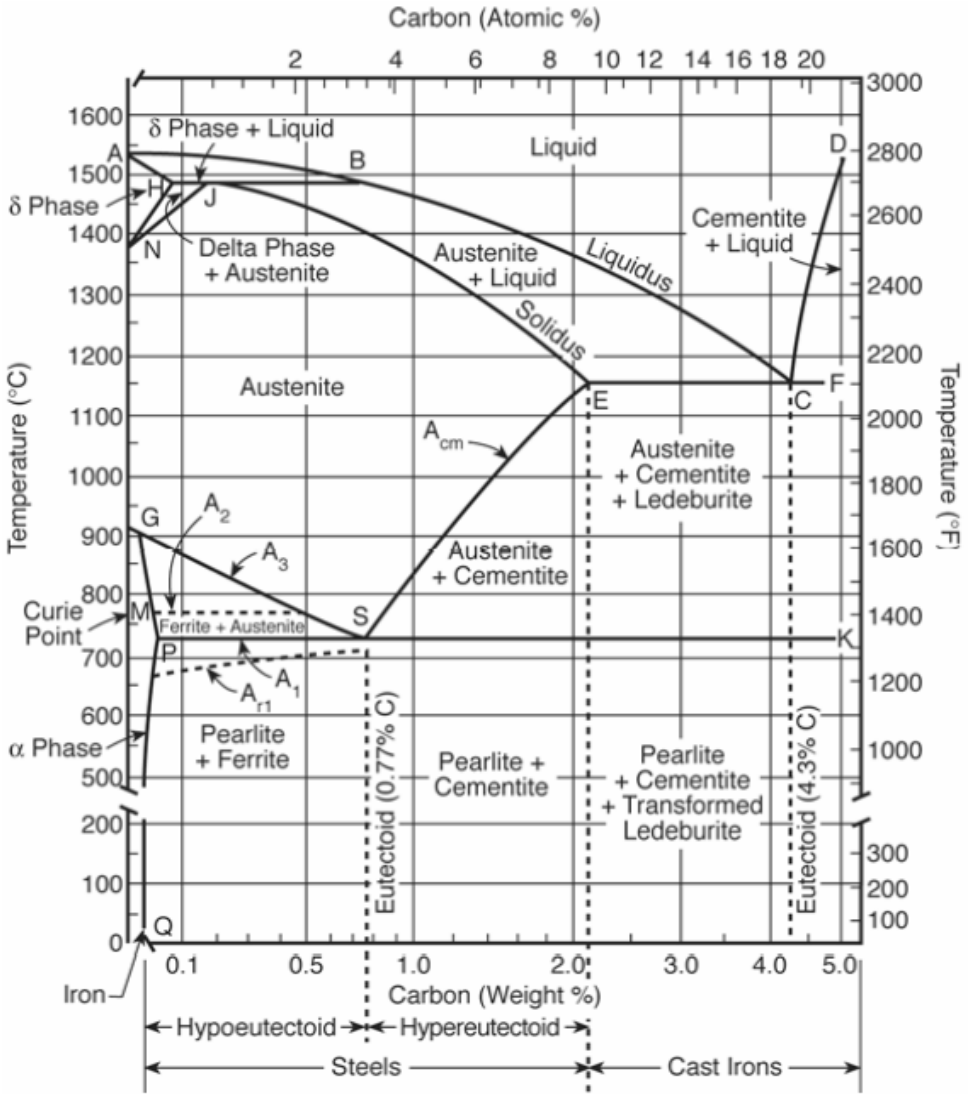


**Figure 2.2.** The iron-iron carbide phase diagram [34].

will have a transformation temperature range that will vary with the carbon content and heating or cooling rate.

The diagram just depicted in this chapter will help you understand the hypoeutectoid steel and its allotropic forms that we discuss next in the following Section 2.4.

## 2.4 Hypoeutectoid Steel

Hypoeutectoid, or low carbon steel is quite crucial in the manufacturing industry since it meets a wide range of applications; one of its applications is in the production of annealed wire. This section presents a general description of steel, and in particular,

hypoeutectoid steel.

Steel [64] is made by the dissolution of carbon into pure iron. It melts at a high temperature, 1540°C; at these temperatures, carbon dissolves into the molten iron and generates a liquid solution. When the liquid solution gets cold, it generates a solid material, in which the atoms of carbon (C) integrate into the solidified iron. Pure iron in its solid-state has three allotropic forms: austenite (y), ferrite, and epsilon-iron.

The crystalline structure of pure iron is ferrite at room temperature [34]. The room temperature form of ferrite is called alpha ($\alpha$) ferrite (see Figure 2.2). The ferritic structure is unstable at high temperatures and transforms into another structure called gamma ($\gamma$) austenite. The austenitic structure might again transform into the form of ferrite at even higher temperatures. This is called delta ($\delta$) ferrite.

The single atoms of carbon place into the spaces between the iron atoms of the crystalline grains, depending on the temperature, of austenite (at high temperatures) or ferrite (at low temperatures). When the percent of carbon dissolved in the molten iron keeps below 2.1% weight, the resulting material is steel. As stated in Section 2.1, in addition to carbon, all modern steels contain the element manganese (Mn) and silicon (Si), and they may contain some amount of sulfur atoms (S) and phosphorus (P), which are impurities.

From [64] we have:

"Steels can be thought of as alloys of three or more elements, given as Fe _ C _ X, where Fe and C are the chemical element symbols for iron and carbon, and X can be thought of as third-element additions and impurities. Most steels are classified by a code developed by the American Iron and Steel Institute (AISI). It is customary to partition steel compositions into two categories: plain carbon steels and alloy steels. In plain carbon steels, X consists only of manganese, sulfur, and phosphorus, whereas in alloy steels, one or more additional alloying elements are added".

In Figure 2.3 we see the different steel grades according to their chemical composition.

The Fe-C phase diagram depicted in Figure 2.2 illustrates an essential characteristic in the steel composition range which is called the 'eutectoid point' [1]. This point relates to

| UNS No. | SAE No. | Chemical Composition Limits, %[1][2] C | Chemical Composition Limits, %[1] Mn | Chemical Composition Limits, %[1] P, Max | Chemical Composition Limits, %[1] S, Max |
|---|---|---|---|---|---|
| G10020[4] | 1002[4] | 0.02–0.04 | 0.35 Max | 0.030 | 0.050 |
| G10030[4] | 1003[4] | 0.02–0.06 | 0.35 Max | 0.030 | 0.050 |
| G10040[4] | 1004[4] | 0.02–0.08 | 0.35 Max | 0.030 | 0.050 |
| G10050[5] | 1005[5] | 0.06 Max | 0.35 Max | 0.030 | 0.050 |
| G10060*[5] | 1006[5] | 0.08 Max | 0.25–0.40 | 0.030 | 0.050 |
| G10070[4] | 1007[4] | 0.02–0.10 | 0.50 Max | 0.030 | 0.050 |
| G10080*[5] | 1008[5] | 0.10 Max | 0.30–0.50 | 0.030 | 0.050 |
| G10090[5] | 1009[5] | 0.15 Max | 0.60 Max | 0.030 | 0.050 |
| G10100 | 1010 | 0.08–0.13 | 0.30–0.60 | 0.030 | 0.050 |
| G10120 | 1012 | 0.10–0.15 | 0.30–0.60 | 0.030 | 0.050 |
| G10130 | 1013 | 0.11–0.16 | 0.30–0.60 | 0.030 | 0.050 |
| G10150 | 1015 | 0.13–0.18 | 0.30–0.60 | 0.030 | 0.050 |
| G10160 | 1016 | 0.13–0.18 | 0.60–0.90 | 0.030 | 0.050 |
| G10170 | 1017 | 0.15–0.20 | 0.30–0.60 | 0.030 | 0.050 |
| G10180 | 1018 | 0.15–0.20 | 0.60–0.90 | 0.030 | 0.050 |
| G10190 | 1019 | 0.15–0.20 | 0.70–1.00 | 0.030 | 0.050 |
| G10200 | 1020 | 0.18–0.23 | 0.30–0.60 | 0.030 | 0.050 |
| G10210 | 1021 | 0.18–0.23 | 0.60–0.90 | 0.030 | 0.050 |
| G10220 | 1022 | 0.18–0.23 | 0.70–1.00 | 0.030 | 0.050 |
| G10230 | 1023 | 0.20–0.25 | 0.30–0.60 | 0.030 | 0.050 |
| G10250 | 1025 | 0.22–0.28 | 0.30–0.60 | 0.030 | 0.050 |
| G10260 | 1026 | 0.22–0.28 | 0.60–0.90 | 0.030 | 0.050 |
| G10290 | 1029 | 0.25–0.31 | 0.60–0.90 | 0.030 | 0.050 |
| G10300 | 1030 | 0.28–0.34 | 0.60–0.90 | 0.030 | 0.050 |
| G10330 | 1033 | 0.30–0.36 | 0.70–1.00 | 0.030 | 0.050 |
| G10350 | 1035 | 0.32–0.38 | 0.60–0.90 | 0.030 | 0.050 |
| G10370 | 1037 | 0.32–0.38 | 0.70–1.00 | 0.030 | 0.050 |
| G10380 | 1038 | 0.35–0.42 | 0.60–0.90 | 0.030 | 0.050 |
| G10390 | 1039 | 0.37–0.44 | 0.70–1.00 | 0.030 | 0.050 |
| G10400 | 1040 | 0.37–0.44 | 0.60–0.90 | 0.030 | 0.050 |
| G10420 | 1042 | 0.40–0.47 | 0.60–0.90 | 0.030 | 0.050 |

**Figure 2.3.** Table of SAE J405 steels by their chemical composition.

the composition of a solid phase that transforms into two or more phases after cooling. For carbon steel, the eutectoid point happens at 0.77 wt. % carbon. This scheme is, in fact, the basis of steel classification into hypoeutectoid, eutectoid, and hypereutectoid steels.

Considering the above description of steel, in summary, we can define the hypoeutectoid steels as those steels with less than $\sim 0.80$ wt. (strictly 0.77 wt. %) carbon.

The mechanical properties of steels depend upon some properties inherent to the material microstructure and the chemical composition whose scheme was explained. Now we need to describe those mechanical properties in the next section.

## 2.5 Mechanical Properties

In what concerns the mechanical properties of the metals, we learn from [64] that "the most important properties of metals that account for their widespread use are their mechanical properties. These properties include a combination of very high strength with the ability to bend rather than break. Various tests have been developed to characterize the strength and ductility (a measure of bendability) of metals and other materials. The majority of such tests [7] used to characterize the mechanical properties of steel are discussed in this chapter. For the Tensile Test [15] consider the simple example of pulling apart a small spring a fair amount and then releasing it. The spring springs back to its original length. Now, repeat the process, but this time, pull on the spring and extend it by a large amount. As the spring becomes overextended relative to its design, the increasing force needed to continue extending the spring suddenly drops, and the spring somewhat "gives." When the spring is released, it does not return to its original length. The spring is now permanently stretched to a longer length and probably ruined, at least for its intended purpose. It has been developed a test to evaluate the strength of metals that is related to this simple experiment. A length of the metal, usually a round cylindrical rod, is pulled apart in a machine that applies a known force, $F$. The machine has grips attached to the ends of the cylindrical metal rod, and the force is applied parallel to the axis of the rod. As the force increases, the rod gets longer, and the change in length is represented as $\Delta l$, where the symbol $\Delta$ means "a change in," and the $l$ refers to the original length of the rod. A force of 100 pounds is applied to two rods of the same material, where one is thin and the other thick. The thin rod will elongate more. To compare their mechanical properties independent of rod diameter, engineers define a term called stress, which is simply the force divided by the cross-sectional area of the rod. When the same stress is applied to the thin and thick rods, they elongate the same amount, because the actual force applied to the thick rod is now larger than that applied to the thin rod by an amount proportional to its larger area. Because stress is force per area, it has units of pounds per square inch (psi), or, more commonly, kpsi. The symbol "k" for kilo means 1000 times, so 1 ksi equals _1000 psi, or 1000 pounds per square inch. For example, 50 ksi is the same as 50,000 psi".

## 2.6 Wire Drawing Process

Drawing operations involve the forcing of metal through a center holed cylinder, called a die, using a tensile force applied axially to the outer side of the die [31]. Compression force causes most of the plastic flow and arises from the opposite reaction of the metal with the die. Usually, the metal has circular symmetry, but this is not an absolute

requirement. Wire drawing reduces the diameter of a solid bar or rod by successive reduction steps, depending on the desired diameter of the final product (commercial wire drawing usually starts with a coil of hot-rolled 5.5 - 9 mm diameter wire). This process is usually performed at room temperature, and is thus classified as a cold working process. However, there is considerable temperature increase during the drawing operation because large deformations are typically involved. Figure 2.4 shows the cross-section through a typical drawing die.

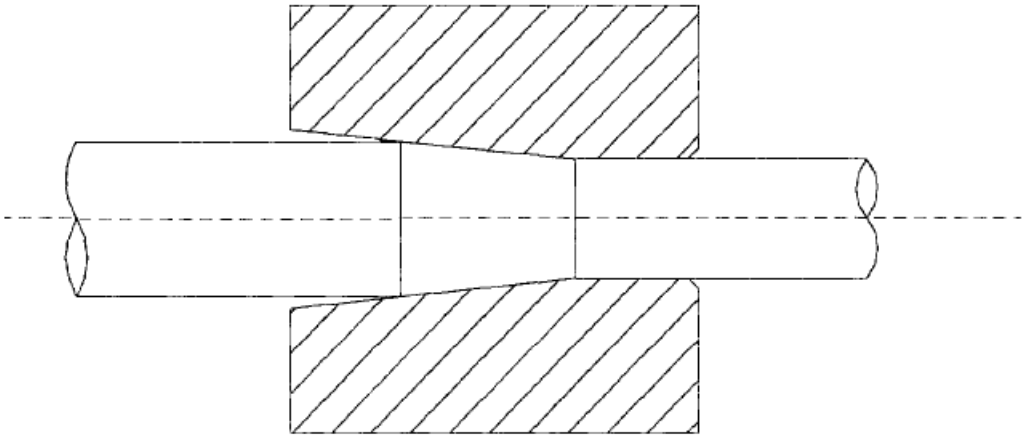

**Figure 2.4.** Cross section of a typical drawing die [16].

While the wire is pulled through the die [65], its volume does not change, so as the diameter decreases, the length increases. Usually, the area reduction in small wires comes from 15-25%, while in larger ones, it is about 20-45%. The process of wire drawing modifies the material's mechanical properties due to the cold working. For some final applications, it must be annealed. We describe the annealing process next in the following section. To have a broader explanation of the wire drawing process, please refer to [30].

## 2.7 Annealing Process

During ASTM A510/A853 [8], [9] wire drawing production processes, microscopic shifting takes place in the material structure. The steel grain enlarges axially. This shifting shows up as important changes in its macroscopic properties mainly because tensile stress increments drastically. To recover the micro-structure and make the material workable again, it is subjected to a heat treatment known as annealing. In this process [22], [57] the steel wire overheats up to around 800 - 850°C. In the interim, the distorted lattice structure (because of the cold-working) is changed to another strain-free

structure, (see Figure 2.5).

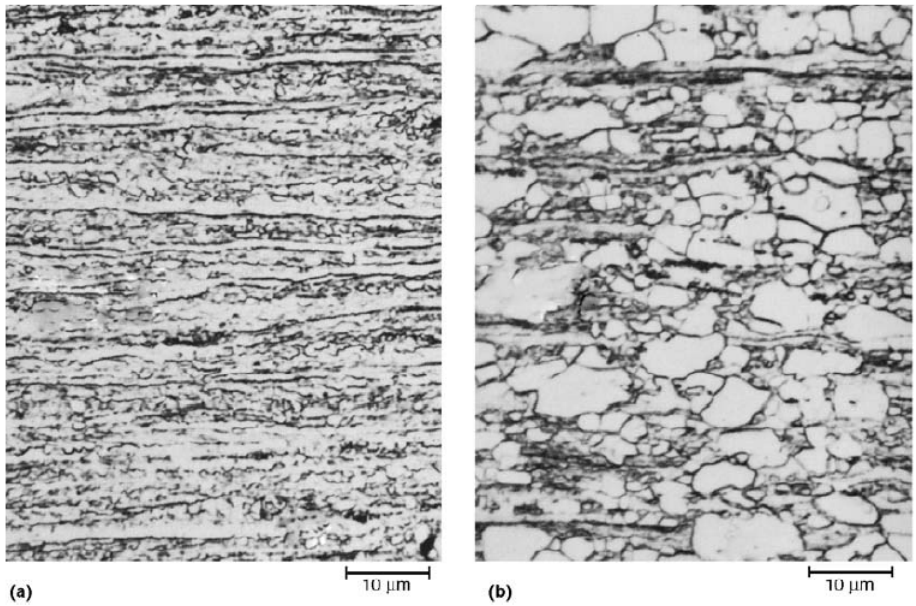


**Figure 2.5.** Distorted micro-structure [64] after the cold-drawn process (a). Restored micro-structure after the annealing process (b).

This process is carried out entirely in the solid-state and is usually followed by slow cooling in the furnace [56]. There exists a continuous annealing process, in which the steel wire receives heat individually [22], and batch annealing where the steel wire coils are located together in a furnace and are overheated normally between 3 and 6 hours, (see Figure 1.1 on Section 1). Oxidation happens during this time and is what generates the scale on the surface of the finished product.

## 2.8 Metallography

Metallography is the study of the physical microstructure and constituents of metals, using microscopy, [14]. It has to do with the composition and structure, and the way it relates to the properties of metals and alloys. Many metallic materials properties [52], such as yield strength, coercivity, thermal conductivity, and corrosion resistance, are more or less related to the microstructure. The relationship between the material's microstructure and its properties become very important in controlling and developing metals. Metallography is the examination of the microstructure. It is an important test method for producing steel and is a powerful tool to detect manufacturing defects and failures in materials. Without a doubt, most investigations are carried out with incident

light microscopy to reveal the various microstructural features (see Figure 2.5).

There are two examination methods in metallography: macroscopy and microscopy.

Macroscopy [5] is an inspection of a metal or an alloy performed under 10x, by the naked eye, or by a low-power microscope. Macroscopy examination techniques [63] are frequently employed in routine quality control, failure analysis, and research. These techniques are generally preliminar to a microscopic examination; however, they serve by themselves as a criterion for acceptance or rejection in quality control. A great variety of destructive and non-destructive procedures are available. The most basic method involves simple visual examination for surface features such as seams, laps, or scales. In Figure 2.6 an example of a macroscopy test (0.5x), we see the flow lines of a forged steel hook; the flow lines show the direction of metal flow during the processing and frequently represent paths for uncomplicated fracture.

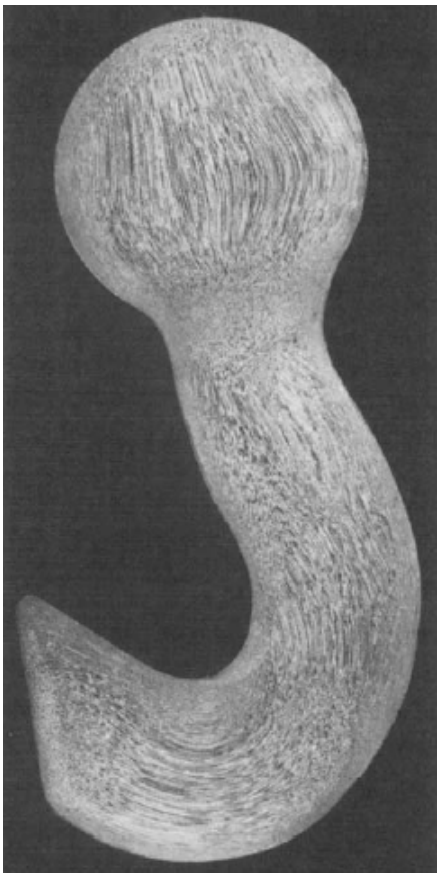

**Figure 2.6.** Flow lines in a forged steel hook [47].

In microscopy [5], an equivalent examination is performed with prepared samples of metal. It can be done by employing magnifications with the optical microscope from about 100x to as high as 2000x. The most important application is the characterization of the structural phases present and the constitution of the bulk of the metal. (The structure of metals consists of the phases as modified by the processing and the mode and manner of the phase distribution, compositions, and characteristics.)

The observations obtained from this test [24] comes to have practical importance because the structure and constitution have a remarked dependence on the material's behavior. In these studies, researchers examine the surface of a properly prepared material. An example is in Figure 2.5, which shows the microstructure of a steel wire drawn before and after being annealed. Another common application of microscopy is determining the average grain size in crystalline materials [10].

For a broader explanation of these examination tests, please refer to [47]. Once presented with the materials, processes, and tests on which we will perform the mathematical model, we can continue to the next chapter to establish the theoretical framework that will be resorted to in order to raise our oxidation model.

# CHAPTER 3
# THEORETICAL FRAMEWORK

This chapter examines the basis on which we are building this research work. At first, there is presented the implied mathematical background that serves as the foundation for developing the model that describes the oxidation phenomenon (as an isothermal and non- isothermal instance). Afterward, it exhibits the fundamental laws that govern oxidation phenomenon kinetics, as well as the thermodynamics that are involved. Then in the next chapter, those foundations will be applied as a non-isothermal oxidation case to the steel coils inside the furnace during the annealing process.

## 3.1 Mathematics

### 3.1.1 Differential Equations

The mathematical models that we raise in this work are primarily formulated upon continuously differentiable functions. Various problems arise in connection to differential equations; we resort to differential equations to work up the rate of change of the phenomenon. This section presents a brief introduction of differential equations of the kind used in this section and the next one.

In natural sciences and engineering, mathematical models are helpful to better understand physical phenomena. Frequently, these models produce an equation that contains some derivatives [60] of an unknown function. This kind of equation is a differential equation [49]. Examples of such equations are the next ones.

Newton's Second Law of Motion; states that the force $F$ over a falling object equals its mass times its acceleration, and it could be expressed by the equation:

$$m\frac{dv}{dt} = F, \tag{3.1}$$

where $m$ is the object mass, and $\frac{dv}{dt}$ the first derivative with respect to time, represents the acceleration employing the velocity.

The two-dimensional heat flow over a body [37], for steady state, with no heat generation:

$$\frac{\partial^2 T}{\partial x^2} + \frac{\partial^2 T}{\partial y^2} = 0, \tag{3.2}$$

where $T$ represents the object temperature, and $x$, $y$ the directions over the heat flow. This one is best known as the Laplace equation.

A differential equation that only implies ordinary derivatives concerning just one independent variable is called an ordinary differential equation [49]. A differential equation that implies partial derivatives with respect to more than one independent variable is called a partial differential equation [27], [66]. In the present chapter and the next one, we will be working with both ordinary and partial differential equations. In the above examples, (3.1) is an ordinary differential equation, while (3.2) is a partial differential equation.

Another classification is the order of a differential equation [59]. This is the maximum order of the derivatives that appear in the equation. In the above examples, (3.1) is of the first order, while (3.2) is of the second order; in the present chapter and the next one, we will be working with first-order derivatives.

The last classification is whether these are linear or nonlinear [19]. A differential equation is that in which the dependent variable and their derivatives only appear as an additive linear combination of their first powers, this is, if they have the format:

$$a_n(x)\frac{d^n y}{dx^n} + a_{n-1}(x)\frac{d^{n-1} y}{dx^{n-1}} + \cdots + a_1(x)\frac{dy}{dx} + a_0(x)y = F(x), \tag{3.3}$$

where $a_n(x)$, $a_{n-1}(x)$, ...,$a_0(x)$ and $F(x)$ depends only on the independent variable $x$. One equation that is not in the form of (3.3), is named a nonlinear equation [66]. In the above examples, (3.1) is a linear differential equation, while (3.2) is a nonlinear one. In the present chapter as well as in the next one, we will be working with linear differential equations.

Now that an overview of the differential equations we will be working with in this thesis has been presented, it is time to introduce the Moore-Penrose Pseudoinverse. We will see it in the next chapter.

### 3.1.2 Moore-Penrose Pseudoinverse

The Moore-Penrose pseudoinverse will be needed to calculate a proposed parameter that is let us suppose we have a linear equation system to solve, but we have more equations

than variables. The system is:

$$A\vec{x} = \vec{y},$$

where $\vec{x}$ and $\vec{y}$ are vectors and $A$ is a matrix. Suppose that we know $A$ and $\vec{y}$, and need to find $\vec{x}$. If $A$ were a square matrix, we could go ahead in the following way:

$$\begin{aligned} \vec{y} &= A\vec{x} \\ A^{-1}\vec{y} &= A^{-1}A\vec{x} \\ A^{-1}\vec{y} &= I\vec{x} \\ A^{-1}\vec{y} &= \vec{x}. \end{aligned}$$

Since $A$ is not squared, the usual inverse $A^{-1}$ cannot be calculated; however, a pseudo inverse $A^{\dagger}$ can come to the aid. A solution to this problem involves the Moore-Penrose pseudoinverse $A^{\dagger}$. We would have:

$$\begin{aligned} A^{\dagger}A &\approx I \\ \text{but } \ AA^{\dagger} &\neq I \ \text{ (unless } A^{\dagger} \text{ is the usual inverse)} \end{aligned}$$

Then the way to proceed would be:

$$\begin{aligned} \vec{y} &= A\vec{x} \\ A^{\dagger}\vec{y} &\approx A^{\dagger}A\vec{x} \approx I\vec{x} \\ A^{-1}\vec{y} &\approx \vec{x} \end{aligned}$$

First of all, we need to define the Moore-Penrose pseudoinverse.

**Definition 3.1.** *Let $A$ be a m x n matrix over $\mathbb{F}$, where $\mathbb{F}$ is a field of the reals $\mathbb{R}$ or the complex $\mathbb{C}$ numbers. There exists a unique n x m matrix $A^{\dagger}$ over $\mathbb{F}$ that satisfies the following criteria, known as the Moore-Penrose conditions [35]:*

1. $AA^{\dagger}A = A$,
2. $A^{\dagger}AA^{\dagger} = A^{\dagger}$,
3. $\left(AA^{\dagger}\right)^{*} = AA^{\dagger}$,
4. $\left(A^{\dagger}A\right)^{*} = A^{\dagger}A$.

*$A^{\dagger}$ is called the Moore-Penrose pseudoinverse.*

When $(A^*A)^{-1}$ exists, the Moore-Penrose can be found in the following way:

$$A^\dagger = (A^*A)^{-1} A^*.$$

Regardless of whether a matrix is a square or full range, the pseudoinverse will always exist. The pseudoinverse is frequently applied to solve least squares systems, using the equation $Ax = b$. When $b$ is not in the range of $A$, there are solutions to the system, but it is desirable to find an $x_0$ closest to a solution. In this case, if $A^\dagger$ is a pseudoinverse, then $A^\dagger b$ provides a vector $x_0$ that minimizes $||Ax - b||$.

**Definition 3.2.** *A solution by least squares to a system $Ax = b$, is a vector such that:*

$$||Ax_0 - b||^2 = ||Ax - b||^2 + ||e||^2$$

*generates the smallest possible error $e$.*

A solution by least squares [42] is found when $x_0$ generates a minimum value in the norm of the residual vector $r_0$.

**Theorem 3.3.** *$x_0 = A^\dagger b$ is the best approximate solution to the system $Ax = b$.*

*Proof.* Let $x \in \mathbb{C}^m$; We can express $Ax = b$ in the following way:

$$Ax - b = A(x - A^\dagger b) + (I - AA^\dagger)(-b)$$

by applying the Pythagorean theorem and the norm on both sides, it can be deduced:

$$\begin{aligned} ||Ax - b||^2 &= ||A(x - A^\dagger b)||^2 + ||(I - AA^\dagger)(-b)||^2 \\ &= ||A(x - x_0)||^2 + ||Ax_0 - b||^2 \\ &\geq ||Ax_0 - b||^2. \end{aligned}$$

□

Then the norm of the residual vector $r_0$ reaches its minimum value when $x = x_0$.

### 3.1.3 Tikhonov Regularization

The Tikhonov regularization will also be needed to calculate the proposed parameter that we will introduce in Chapter 4, so here is a valuable theory for that end. Tikhonov

regularization [43] is a method to address badly posed problems, in the sense that well-posed problems exhibit the following features:

1. Own just one solution.
2. The solution is unique.
3. The solution changes to the same extent as the initial conditions change.

Let us define the regularized Tikhonov solution:

**Definition 3.4.** *(Regularized Tikhonov [42] solution). Let $\alpha > 0$ a constant. The regularized Tikhonov solution is a vector $x \in \mathbb{R}^n$ that minimizes:*

$$arg\,min_x T_\alpha(x) = \frac{1}{2}||Ax - y||^2 + \frac{\alpha}{2}||x||^2$$

*provided that such minimizer exists. The $\alpha$ parameter is called the regularization parameter.*

Definition (3.4) can be understood as a balance between two requisites:

1. $x$ it must throw a small residual error in $Ax - y$, and
2. $x$ it must be small on the $L^2$ norm.

The election of priority of each parameter is set with the $\alpha$ parameter.

Before continuing, it is important to point out the following; if we needed to calculate the Hessian matrix of $T_\alpha(x)$, it would be:

$$T_\alpha(x) = \frac{1}{2}||Ax - b||^2 + \frac{\alpha}{2}||x||^2,$$

and then

$$\begin{aligned}
\nabla T_\alpha(x) &= \frac{1}{2}\sum_{i=1}^{n}\frac{\partial}{\partial x_k}\left(\left(\sum_{j=1}^{n}a_{ij}x_j - b_i\right)\right)^2 + \frac{\alpha}{2}\sum_{j=1}^{n}\frac{\partial}{\partial x_k}x_j^2 \\
&= \frac{1}{2}\sum_{i=1}^{n}2\left(\left(\sum_{j=1}^{n}a_{ij}x_j\right) - b_i\right)(a_{ik}) + \frac{\alpha}{2}(2x_k) \\
&= \sum_{i=1}^{n}\left(\left(\sum_{j=1}^{n}a_{ij}x_j\right) - b_i\right)(a_{ik}) + \alpha x_k \\
&= (Ax-b)A^* + \alpha I x \\
&= A^*Ax - A^*b + \alpha I x \\
&= (A^*A + \alpha I)x - A^*b,
\end{aligned}$$

where $A^*$ in this case, is the transpose of the $A$ matrix.

Returning to the description of the Tikhonov regularization, the following theorem shows that definition (3.4) is well-grounded.

**Theorem 3.5.** *Let $A : \mathbb{R}^n \longrightarrow \mathbb{R}^m$ be a compact operator with singular value decomposition. Then the regularized Tikhonov solution exists, is unique and is given by:*

$$x = \left(A^*A + \alpha I\right)^{-1} A^*y \tag{3.4}$$

*Proof.* If the gradient of $T_\alpha$ is calculated and equaled to zero, it would be [35]:

$$\begin{aligned}
0 &= \nabla T_\alpha(x), \\
&= A^*(Ax - y) + \alpha I x, \\
&= A^*Ax - A^*y + \alpha I x, \\
&= (A^*A + \alpha I)x - A^*y.
\end{aligned}$$

from which we have:

$$x_\alpha = \left(A^*A + \alpha I\right)^{-1} A^*y,$$

that is known as the least squares solution to the minimum norm. Now let $\psi = (A^*A + \alpha I)$ be a n x n matrix, and let $\alpha > 0$ be big enough such that $\psi$ be a positive-defined matrix.

First of all, it is hold:

$$\psi \cdot adj(\psi) = det(\psi) I_n$$

where $adj(\psi)$ is the adjoint matrix of $\psi$; then:

$$\psi \left( \frac{1}{det(\psi)} adj(\psi) \right) = I_n$$

such that $\frac{1}{det(\psi)} \cdot adj(\psi)$ is the inverse of $\psi$. Now suppose that the inverse of $\psi$ does not exist.

$$\Rightarrow det(\psi) = det(A^*A + \alpha I) = 0$$

On the other hand we know

$$det(A^*A + \alpha I) = c_n \alpha^n + \cdots + c_\alpha + c_0$$

that is a polynomial. By the fundamental theorem of algebra, there exist at most $n$ real roots $r_1, r_2, ..., r_k$ with $k \leq n$. Then we can choose a big enough $\alpha$ value e.g.:

$$\alpha = max\{r_1, ..., r_k\} + 1000$$

such that it satisfies $det(A^*A + \alpha I) > 0$. □

How can we properly select the regularization parameter $\alpha > 0$?. Unfortunately, this is a question that remains unsolved in general. However, some methods exist to pick $\alpha$, as in Morozov's discrepancy principle. If we have an error estimator based on data, then basically, any solution that outputs a measure with an error with the same magnitude is acceptable.

Suppose that we have a data-based error estimator, for example:

$$||y - y_0|| \simeq \epsilon,$$

for some $\epsilon > 0$. Then any $x \in \mathbb{R}$ such that

$$||Ax - y|| \leq \epsilon$$

should be considered an acceptable approximate solution. Let $x_\alpha$ be defined as in (3.4), and

$$f : \mathbb{R}_+ \longrightarrow \mathbb{R}_+ \ , \ \ f(\alpha) = ||Ax_\alpha - y||,$$

the discrepancy related to the $\alpha$ parameter. Morozov's discrepancy principle [42] states that the regularization parameter $\alpha$ must be selected from the condition

$$f(\alpha) = ||Ax_\alpha - y|| = \epsilon,$$

and if possible, the regularized solution should no satisfy data in a more precise fashion than the noise level.

## 3.2 Physics

### 3.2.1 Thermodynamics

Here we will review the thermodynamic foundations that make it possible for oxidation to take place in the annealing process.

Thermodynamics is a branch of physics that deals with energy, its forms and transformations, and their relation to matter's physical properties. The term thermodynamics [62] comes from the Greek words "therme" (heat) and "dynamis" (power). One of the fundamental laws of the universe is the first law of thermodynamics, which states that during an interaction, or process the total amount of energy remains constant. In other words, energy cannot be created or destroyed. The second law of thermodynamics states that energy poses quality and quantity. This is, a process is performed to decrease the quality of energy. A process cannot take place unless it satisfies both the first and second laws of thermodynamics.

In thermodynamic analysis, the various forms of energy of a system can be considered in two categories: macroscopic and microscopic. The macroscopic forms of energy are the ones a system possesses as a whole regarding outside reference frames, such as kinetic and potential energy. On the other hand, microscopic forms of energy relate to a system's microstructure and the degree of molecular interactions. They do not depend on outside reference frames. The internal energy of a system, denoted by U , represents the sum of all the microscopic forms of energy.

There is a property of a thermodynamic system, enthalpy($H$), which is defined as the sum of a system's internal energy $U$, and the product of its pressure and volume:

$$H = U + PV,$$

where $U$ is the system's internal energy, $P$ is the pressure, and $V$ is the system's volume. The Second Law of Thermodynamics introduces another important physical property that is most commonly associated with a state of disorder, randomness, or uncertainty of a system. It can also be seen as the measure of the energy dispersed in a process [17]. The definition of entropy (thermodynamically) deals with the change in this property, $dS$, which generally comes from physical or chemical changes (due to a process). The definition is motivated by the question of how much energy can be converted to work or transferred as heat.

Entropy is a somewhat abstract property, and it is not easy to give a physical description of it. We will formally define entropy, but first we will compare two expressions for the efficiency of a simple reversible heat engine that operates between two reservoirs at the temperatures $\theta_1$ and $\theta_2$. Suppose we run the engine with the high-temperature reservoir at some time, a quantity of heat $Q$ will flow from this reservoir and a positive amount of work will be generated. Empirically researchers found that if a heat engine operates between two temperature reservoirs and a positive amount of work is generated, then $Q_1$ the heat withdrawn from the high-temperature reservoir is positive, whereas $Q_2$, and the heat withdrawn from the low-temperature reservoir is negative. The negative value of $Q_2$ means that the heat goes to the low-temperature reservoir.

By [25], [58] the efficiency $\epsilon$ of an engine operating this way is given by:

$$\epsilon = 1 + \frac{Q_2}{Q_1} \quad \text{and} \quad \epsilon = 1 + \frac{\theta_2}{\theta_1}.$$

After subtracting these two expressions, it yields the result

$$\frac{Q_2}{Q_1} + \frac{\theta_2}{\theta_1} = 0,$$

which can be rearranged to the form

$$\frac{Q_1}{\theta_1} + \frac{Q_2}{\theta_2} = 0. \tag{3.5}$$

The left-hand side of (3.5) is simply the sum over the cycle of the quantity $Q/\theta$. It could be written as the cyclic integral of the differential quantity $dQ/\theta$ :

$$\oint dQ/\theta = 0 \text{ reversible cycles.}$$

Since the sum over the cycle of the quantity, $dQ/\theta$ is zero. This quantity is the differential of some property; this property is called the *entropy* of the system. The symbol $S$ represents it. The definition for entropy is then

$$dS \equiv dQ_{rev}/T, \tag{3.6}$$

where the subscript "rev" in (3.6) indicates the restriction to reversible cycles, and the more usual symbol $T$ has replaced the symbol $\theta$ for the thermodynamic temperature. The term $dQ_{rev}/T$ can be viewed as the sum of all the differential amounts of heat transfer (to or from a system) divided by the temperature. As a system becomes disordered, the positions of the molecules become less predictable, and the entropy increases.

There is a thermodynamic potential that can be used to calculate the maximum reversible work that can be exerted by a thermodynamic system at constant pressure and temperature: the Gibbs free energy ($G$). This potential determines the possibility that certain processes can be carried out spontaneously, that is, it can occur.

When a process involves some transformation, like chemical reactions, the system's composition at the end of a process does not remain the same as that at the beginning of such a process. In this case, it becomes a necessity to have a common reference state for all chemical components. By convention, the chosen reference state is 25°C and 1 atm, which is known as the standard reference state. A superscript indicates property values at the standard reference state (°) (such as H° and U°).

Consider the chemical reaction:

$$\mathrm{aA} + \mathrm{bB} \rightarrow \mathrm{cC} + \mathrm{dD}$$

The free Gibbs energy for a chemical reaction like the one described above is defined by [26]:

$$G \equiv H - TS,$$

where $H$, $T$, and $S$ represent the reaction enthalpy, entropy, and temperature, respectively. In a simplified context, it can be assumed that $H$ and $S$ are pressure and temperature-independent; however, for a more exact result, it can be represented as

$$nG^{\circ} = f(P, T, n_1, n_2, ..., n_i, ...),$$

as a function of the whole variables mentioned above and the number of moles ($n$) of the individual species [25].

$$d(nG^\circ) = \Big[\frac{\partial(nG^\circ)}{\partial P}\Big]_{T,n} dP + \Big[\frac{\partial(nG^\circ)}{\partial T}\Big]_{P,n} dT + \sum_i \Big[\frac{\partial(nG^\circ)}{\partial n_i}\Big]_{P,T,n_j} dn_i. \tag{3.7}$$

It is held [23] that for a volume of matter $V$:

$$\Big[\frac{\partial(nG^\circ)}{\partial P}\Big]_{T,n} = nV \quad ; \quad \Big[\frac{\partial(nG^\circ)}{\partial T}\Big]_{P,n} = -nS.$$

on the other hand, chemical equilibrium is reached when

$$\sum_i \Big[\frac{\partial(nG^\circ)}{\partial n_i}\Big]_{P,T,n_j} = 0,$$

then define [25] $dH^\circ = TdS^\circ + VdP$ .

After that, by substituting all the above in (3.2) and introducing the integral operator, it is obtained:

$$\int_{G_0^\circ}^{G^\circ} dnG^\circ = \int_{H_0^\circ}^{H^\circ} dnH^\circ - \int_{S_0^\circ}^{S^\circ} TndS^\circ - \int_{T_0}^{T} nS^\circ dT.$$

Since a value $G^\circ$ is sought at certain specific temperature $T_0 = T$, then $\int_{T_0}^{T} nS^\circ dT = 0$. Using integration and division by $n$ on both sides of the equation, yields:

$$\Delta G^\circ = \Delta H^\circ - T\Delta S^\circ, \tag{3.8}$$

that represents the change of the Gibbs free energy; moreover, the above terms can be expressed by

$$\Delta H^\circ = \Delta H_0^\circ + R\int_{T_0}^{T} \frac{\Delta Cp^\circ}{R} dT$$
$$\Delta S^\circ = \Delta S_0^\circ + R\int_{T_0}^{T} \frac{\Delta Cp^\circ}{R}\frac{dT}{T},$$

where $Cp$ is the heat capacity [38] belonging to a body, and it is defined by:

$$Cp = \lim_{\Delta T \to 0} \frac{\Delta Q}{\Delta T},$$

and where $\Delta Q$ represents the heat that must be added to a body to increase its temperature by $\Delta T$.

If the following reaction takes place:

$$\mathrm{aA} + \mathrm{bB} \rightarrow \mathrm{cC} + \mathrm{dD}$$

then $\nu_A = -\mathrm{a}$ , $\nu_B = -\mathrm{b}$ , $\nu_C = \mathrm{c}$ , $\nu_D = \mathrm{d}$, respectively; this way it is possible to represent state functions as:

$$\Delta Cp^\circ \equiv \sum_i \nu_i Cp_i^\circ \quad ; \quad \Delta H_0^\circ \equiv \sum_i \nu_i H_{0i}^\circ \quad ; \quad \Delta S_0^\circ \equiv \sum_i \nu_i S_{0i}^\circ.$$

Substituting the above in (3.8) obtains:

$$\Delta G^\circ = \Delta H_0^\circ + R\int_{T_0}^{T} \frac{\Delta Cp^\circ}{R} dT - T\Delta S_0^\circ - RT\int_{T_0}^{T} \frac{\Delta Cp^\circ}{R}\frac{dT}{T}. \tag{3.9}$$

where

$$\Delta S_0^\circ = \frac{\Delta H_0^\circ - \Delta G_0^\circ}{T_0},$$

represents the Gibbs free energy for a chemical reaction in terms of $H^\circ$ and $S^\circ$ at temperature $T$ with respect to another $T_0$ reference.

Finally, by replacing the above obtained equation in (3.9), the result would be:

$$\Delta G^\circ = \Delta H_0^\circ + R\int_{T_0}^{T} \frac{\Delta Cp^\circ}{R} dT - \frac{T}{T_0}\left(\Delta H_0^\circ - \Delta G_0^\circ\right) - RT\int_{T_0}^{T} \frac{\Delta Cp^\circ}{R}\frac{dT}{T}. \tag{3.10}$$

If the Gibbs free energy is determined for chemical transformation, the following possibilities may take place [23], according to its $\Delta G^\circ$ value:

- $\Delta G^\circ < 0$ The transformation may take place spontaneously.
- $\Delta G^\circ = 0$ The system is in equilibrium with respect to this transformation.
- $\Delta G^\circ > 0$ The transformation is not spontaneous and will not take place; the natural direction is the opposite of this transformation as it is proposed.

In the addressed phenomenon in this thesis, oxidation, we have that $\Delta G^\circ < 0$, so that the transformation or the conversion of iron molecules into iron oxide molecules occurs spontaneously in the furnace while the annealing process is running. As we have seen in

this chapter, the oxidation of iron is possible thermodynamically. However, thermodynamics does not tell us at all the reaction rate, so that so far, we still could not know the scale layer thickness we will have on a steel sample upon heating completion. To make it possible to predict this, we need to go deep into the kinetics of the reaction; that is just what we will see in the next section.

## 3.3 Chemistry

### 3.3.1 Arrhenius Equation

The Arrhenius equation describes the constant rate dependence of a reaction on temperature [26]. The equation has been widely used as a model of the temperature effect on the rate of chemical reactions [6] and biological processes [51]. It has even been successfully applied to numerous reactions involving solids [36].

Consider the following reaction:

$$A \rightarrow B$$

According to collision theory, [17], [23], the rate of change in the molar concentration of $A$ molecules is the product of the collision density and the probability that a collision occurs with sufficient energy. Thus, the reaction rate is directly proportional to the $[A]$ concentration, that is

$$\begin{aligned} rate &\propto [A] \\ &= k[A], \end{aligned}$$

where the term $k$ is known as the rate constant, a proportionality constant between the reaction rate and the concentration of reactants.

In 1889, based on experimental work, Svante Arrhenius came up with an expression for the rate constant of a reaction, given as follows [45], [46]:

$$\left(\frac{\partial \ln k}{\partial T}\right)_P = \frac{E_a}{RT^2}, \tag{3.11}$$

at constant pressure $P$. Integration of (3.11), leads to the common form of the Arrhenius equation:

$$k = A \exp\left(\frac{-E_a}{RT}\right). \tag{3.12}$$

where $E_a$ is the activation energy of the reaction (in kJ/mol) defined as the minimal energy amount required to start a chemical reaction (high activation energy signifies that the rate constant depends strongly on temperature). We represented in Figure 3.1, $R$ is the gas constant (8.314 J/K $\cdot$ mol), $T$ the absolute temperature (in kelvins), and $e$ the base of the natural logarithm. The quantity $A$ represents the collision frequency. That is the average rate at which two reactants collide for a given system and is called the frequency factor; it can be viewed as a constant for a given reacting system over a reasonably wide temperature range. Equation (3.12) shows that the rate constant is directly proportional to $A$ and, therefore, to the collision frequency [26]. In addition, because of the minus sign associated with the exponent $E_a/RT$, the rate constant decreases with increasing activation energy and increases with increasing temperature. Note that a slight change in temperature causes a relatively significant change in $k$, and a change in the value of k is reflected in the rate of reaction. Most rate constants obey the Arrhenius Equation to a good approximation; therefore, this is evidence for collision theory for theoretical reactions.

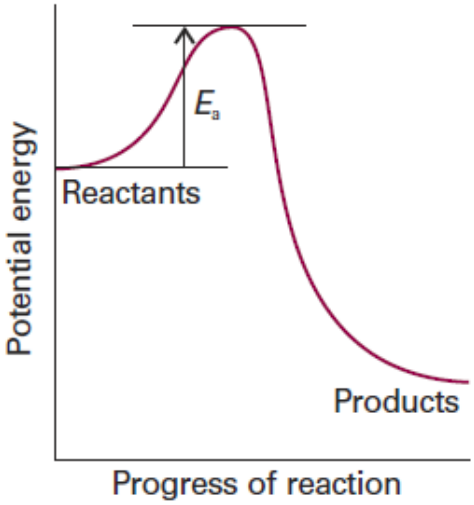


**Figure 3.1.** A potential energy profile for an exothermic reaction. The size of the barrier between the products and reactants is the activation energy of the reaction [17].

Another form of the relation is obtained by taking the natural logarithm of both sides of the equation (3.12):

$$\ln(k) = \ln(A) - \frac{E_a}{R}\left(\frac{1}{T}\right).$$

which is the same as:

$$\ln(k) = \frac{-E_a}{R}\left(\frac{1}{T}\right) + \ln(A).$$

This indeed is the equation of a straight line:

$$y = mx + b.$$

where $x$ is the reciprocal of $T$. So, when a chemical reaction poses a rate constant that obeys the Arrhenius equation, plotting $\ln(k)$ versus $T^{-1}$ throws a straight line, to determine $E_a$ and $A$ we can use its gradient and intercept.

The Arrhenius equation is not derivable from any physical formalism, and it is rooted in experimental observations. This equation can be viewed more as an empirical equation that fits the experimental data in most situations. This equation has been widely accepted [50] and no realistic alternative capable of expressing the $k - T$ relationship or providing an alternative explanation of this pattern of behavior has been accepted [36]. The linearity of the Arrhenius plot, that is, $\ln[k(T)]$ vs. $1/T$, has been traditionally considered evidence of the model's validity [51] since researchers have been observing this behavior experimentally.

### 3.3.2 Kinetics of Oxidation

To properly know the rate of the oxidation reaction, in this section, we will use a tool: kinetics, by applying the Arrhenius equation (3.11) to this reaction. Kinetics is the area of physical chemistry that deals with the rates of chemical reactions [17], [23].

As we have seen in Section 3.2.1, the tendency for a metal to oxidize [57], like any other spontaneous reaction, is indicated by the free energy change $\Delta G$ accompanying the formation of the oxide change $\Delta G$. Most metals readily oxidize because $\Delta G$ is negative for oxide formation. The free energy released by combining a fixed amount (1 mol) of the oxidizing agent with the metal is given by $\Delta G^\circ$. It is usually termed the standard free energy of the reaction. $\Delta G^\circ$ is, of course, related to $\Delta H^\circ$, the standard heat of reaction, and $\Delta S^\circ$ the standard change in entropy, by the Gibbs equation.

The numerical value of $\Delta G^\circ$ for oxidation reactions decreases with an increase in temperature, that is, the oxides become less stable. This process arises from the decreased entropy accompanying the reaction: solid (metal) + gas (oxygen) $\rightarrow$ solid (oxide). The metal and oxide, being solids, have roughly the same entropy values, and

$d(\Delta G)/dT$ is almost equivalent to the entropy of the oxygen.

Changes in the Gibs free energy indicate the more likely stable reaction product, but they do not predict the rate at which a product is generated [21]. While oxidation occurs, the first oxygen molecules absorbed on the metal surface dissociate into their constituent atoms before they link to the atoms of the surface of the metal. This phenomenon is called chemisorption. After a few adsorbed layers are formed, the oxide nucleates epitaxially on the grains of the base metal at propitious sites, such as dislocations and impurity atoms.

The oxide layer [67] on the iron and non-alloyed steel, when annealing in air at temperatures $T > 570\text{C}^\circ$, due to the partial pressure of oxygen and the different valence numbers of iron creates an oxide layer consisting of three different oxides. These oxides are present in a sequence from the one with the lowest amount of oxygen closest to the metal to the one with the highest amount of oxygen closest to the atmosphere: FeO / $Fe_3O_4$ / $Fe_2O_3$ - wüstite / magnetite / hematite. Their relative thickness is mainly constant and not dependent on the thickness of the oxide layer; at $T > 700\text{C}^\circ$ is roughly 95% FeO, 4% $Fe_3O_4$ and 1% $Fe_2O_3$ [61]. At the temperature $T = 570 - 800\text{C}^\circ$ it is, however, possible to find results that deviate in terms of compositions as well as thicknesses of the individual layers, which demonstrates the complexity of the oxidation of iron and non-alloyed steel.

The composition of the three layered oxide layer with a majority of FeO shows that the oxidation at $T > 570\text{C}^\circ$ is controlled by the formation of FeO. A chemical reaction occurs between the iron and the magnetite, creating wüstite:

$$Fe_3O_4 + Fe \rightarrow 4FeO$$

Next, the iron reacts with the hematite, creating magnetite:

$$4Fe_2O_3 + Fe \rightarrow 3Fe_3O_4$$

Because of the constant inflow of oxygen from the air, the hematite never depletes during the formation of magnetite. Hematite is formed when the oxide ions react with the iron ions or with the magnetite. The chemical reactions for the formation of hematite are the

following:

$$2\mathrm{Fe} + 3/2\mathrm{O}_2 \rightarrow \mathrm{Fe}_2\mathrm{O}_3$$
$$2\mathrm{Fe}_3\mathrm{O}_4 + 1/2\mathrm{O}_2 \rightarrow 3\mathrm{Fe}_2\mathrm{O}_3$$

The oxide film formation rate [21] depends on the temperature and the specific material. While growth occurs at low temperatures, since the oxygen atoms gain electrons from the external surface atoms, a strong electric field is formed along with the thin oxide film and pulls the metal atoms through the oxide.

At an intermediate temperature range (e.g., 250–1000°C in Fe), the oxidation develops with time according to a parabolic law $x^2 \propto t$ in almost all metals. In this range, the oxide growth is a thermally-activated process, and ions go through the scale by thermal movement; their rate of migration depends on the structure of the oxide layer lattice. There arise stresses – tensile or compressive – in oxide scale layers that lead to dropping out effects. Continuous breakages on the scale layer may prevent further growth, and the process rate behaves linearly or even faster. These stresses in oxide scale film relate to the Pilling–Bedworth ratio $[PB]$, defined as the proportion of the molecular bulk of the iron oxides to the atomic bulk of the bare metal from which they form. It basically states that the volume of iron oxides is larger than the volume of steel they are formed from.

If $x_{ox}$ is the oxide film thickness in the metal, $\Delta c$ a constant difference concentration of oxygen on the metal and combustion gas interface, and $\mathscr{D}$ a diffusion coefficient, the rate of growth is then given by:

$$dx/dt \propto \mathscr{D}\,(\Delta c/x)\,,$$

and the film thickness, in the temperature ranges approached in this work, grows parabolically [57] according to the relation [44]:

$$\frac{dx_{ox}}{dt} = \frac{K_{ox}}{x_{ox}}, \tag{3.13}$$

where $\mathrm{K}_{ox}$ is a temperature-dependent parabolic rate constant. Many oxides thicken according to a parabolic law over some particular temperature range. Since it is a thermally-activated process, temperature is the most important parameter [61] , and $\mathrm{K}_{ox}$ obeys Arrhenius' law:

$$\mathrm{K}_{ox} = k_0 \exp\left(\frac{-E_a}{RT}\right). \tag{3.14}$$

where $k_0$ is a temperature-independent constant, $E_a$ is the activation energy (depends on both the reaction mechanism and the type of kinetics), $R$ is the universal gas constant (8.314 J/mol K), and $T$ is the oxidation temperature.

At this stage, we have an isothermal model (3.13), (3.14) that describes the rate of growth of the thickness of the oxide scale layer in the surface of a steel sample. Now we are ready to extend this model to the non-isothermal case to achieve scale formation prediction in the batch annealing process, which is the sought-after goal in this work; this will be carried out in the next chapter.

# CHAPTER 4
# MATHEMATICAL MODEL DEVELOPMENT

We raised a mathematical model to predict the growth of the oxide-scale layer in the outer spirals of the steel coils after the material was subjected to the non-isothermal annealing process. In order to achieve it, we consider process variables such as the heating curve (temperature), and the soaking time in the different process stages that usually take place in the industrial process: heating, holding, and cooling. For this work, we assumed that the outside temperature of the drawn wire coil is equal to the furnace atmosphere.

## 4.1 A Model for Isothermal Oxidation

We denote $C'[t_1, t_2]$ as the set of all real-valued differentiable functions. When the coils of steel are subjected to the furnace atmosphere, it suffers oxidation; this is an important phenomenon to consider in the batch annealing process. In the kinetics of oxidation [2], if $x_{ox}(t)$ is the oxide film thickness in the metal, $\Delta c$ a constant difference concentration of oxygen on the metal and combustion gas interface, and $\mathscr{D}$ a diffusion coefficient, as we saw in Chapter 3, the rate of growth would be described by the proportion relation:

$$dx_{ox}(t)/dt \propto \mathscr{D}(\Delta c/x_{ox}(t)).$$

In the temperature range from Table 5.2, the oxide film thickness in iron grows [57], according to the parabolic relation [44]:

$$\frac{dx_{ox}(t)}{dt} = \frac{K_{ox}}{x_{ox}(t)}, \tag{4.1}$$

so that integrating (4.1) between $t = 0$ and $t = t$, and between $x_{ox_0}$ and $x_{ox}$, we obtain

$$\int_{x_{ox_0}}^{x_{ox}} \widetilde{x}_{ox}(t) d\widetilde{x}_{ox} = K_{ox} \int_0^t ds, \tag{4.2}$$

where $K_{ox} \in C'[t_1, t_2]$ is given by the Arrhenius Law [56]:

$$K_{ox} = k_0 \exp\left(-E_a/R\overline{T}\right), \tag{4.3}$$

where $E_a$ is the activation energy, $\overline{T}$ the temperature of the wire, $k_0$ a proportionality constant, and $R$ the universal gas constant.

According to [61], at equilibrium, between $700°C - 1200°C$, the oxide film layer, is composed of:

$$\begin{aligned} \alpha_1 &:= 95\% \leftarrow \text{Wustite FeO/Fe-}\alpha \\ \alpha_2 &:= 4\% \leftarrow \text{Magnetite } Fe_3O_4\text{/Fe-}\alpha \\ \alpha_3 &:= 1\% \leftarrow \text{Hematite } Fe_2O_3\text{/Fe-}\alpha \end{aligned} \tag{4.4}$$

There exists an important relation, handled in these instances [67], the Pilling-Bedworth ratio [PB]: "The volume of iron oxides is larger than the volume of the steel from which they are formed". Given some points $\beta_1, \beta_2, ..., \beta_n \in \mathbb{R}$, this ratio [28] is expressed as the convex combination of those and the coefficients (4.4):

$$[PB] = \sum_{i=1}^{3} \alpha_i \beta_i. \tag{4.5}$$

This way we can obtain the relation:

$$x_{ox}(t) = [PB] x_{metal}(t), \tag{4.6}$$

so that if the steel film thickness from the oxide formed $x_{metal}(t)$ is sought out, from (4.1), (4.3) and (4.6) we would have:

$$x_{metal}(t) = \left( \frac{1}{[PB]^2} k_0 \exp(-Ea/R\overline{T}) \cdot t \right)^{1/2}. \tag{4.7}$$

Since (4.1) is an isothermal kinetic function, and the process performed is non-isothermal, it is necessary to carry out a non-isothermal transformation. The following section deals with such transformation.

## 4.2 A Mathematical Treatment for Non-Isothermal Transformations

We have from [53] the mathematical treatment for non-isothermal transformations; in this section, we briefly explain it, then in the the following section it will be applied to the results from Section 4.1.

Special forms of kinetic differential equations can be established by the following equation and initial condition:

$$\begin{aligned} \frac{dy}{dt} &= f(y,T) \\ y_0 &= y(t_0), \end{aligned} \tag{4.8}$$

that are suitable for the phenomenological description of the transformation processes taking place at varying temperature, where

$f$ = a real-valued differentiable kinetic function.

$t$ = time measured from initial time $t_0$.

$T$ = absolute temperature, so-called state variable of process.

$y$ = extent of completion of process after lapse of time $t$.

$y_0$ = extent of completion of process at initial time $t_0$.

The parameter $y$ may represent, for example, the relative amount of transformed phase or its average size, but it may also represent hardness or another measurable characteristic of the alloy. The kinetic differential equation (4.8) contains the assumption concerning the process kinetics that the instantaneous rate of transformation is influenced exclusively by two factors: the extent of completion of the process $y$ and the temperature $T$. The solution

$$y(t) = y_0 + \int_{t_0}^{t} f(y,T)ds, \tag{4.9}$$

of the kinetic differential equation is called the generalized kinetic function. Equation (4.9) supplies, for the appropriately selected temperature functions $T_1(t)$, $T_2(t)$, ..., the solution functions $y_1(t)$, $y_2(t)$, ..., which are called the representations of the kinetic process.

The traditional isothermal kinetic functions

$$F(t,y,T) = 0, \tag{4.10}$$

may be used to derive the generalized kinetic functions, where $F(t,y,T)$ is a real-valued differentiable kinetic function [23], [17]. The generalized kinetic functions can be gener-

ated using the isothermal kinetic function in equation (4.10). As a first step, suppose that equation (4.10) may be written in the form

$$F(t, y, T) = F_a(y) - K(T)t = 0, \tag{4.11}$$

where $F_a$ is an appropriately selected real function, and where the limiting restrictions

$$\frac{\partial F_a(y)}{\partial t} = \frac{\partial F_a(y)}{\partial T} = \frac{\partial K(T)}{\partial t} = 0,$$

are fulfilled for the functions $F_a$ and $K$. Then, we can conclude that $F_a$ is time and temperature-independent, and $K$ is time-independent. From (4.11), we have:

$$\left(\frac{\partial F}{\partial t}\right)_{y,T} = -K(T) \tag{4.12}$$

$$\left(\frac{\partial F}{\partial y}\right)_{t,T} = \frac{\partial F_a}{\partial y} \tag{4.13}$$

Appealing to the chain rule in $dy/dt$, and substituting the time-temperature function $T(t)$ and (4.12),(4.13) into the resulting differential equation, we obtain the generalized kinetic differential equation:

$$\begin{aligned} \frac{\partial F}{\partial y}\cdot\frac{dy}{dt} &= \frac{\partial F}{\partial t} \\ \frac{dy}{dt} &= -\left.\frac{\frac{\partial F}{\partial t}}{\frac{\partial F}{\partial y}}\right|_{T=T(t)} \\ &= K(T)\left(\frac{\partial F_a}{\partial y}\right)^{-1}. \end{aligned} \tag{4.14}$$

which we sought. This has the special property of being separable with respect to the temperature and the variable $y$:

$$\int_{y_0}^{y}\left(\frac{\partial F_a}{\partial y}\right)d\tilde{y} = \int_{t_0}^{t} K(T)ds. \tag{4.15}$$

Transformation processes that may be described by the generalized kinetic differential equation of the separable type (4.14) shall be termed additive transformation processes, and the kinetics obtained by integrating equation (4.14) shall be termed generalized

additive kinetic functions.

Assuming that the inverse $F_a^{-1}$ of the function $F_a$ exists, after integrating (4.15) the corresponding generalized additive kinetic function can be generated in the form:

$$y(t) = F_a^{-1}\left(\int_{t_0}^{t} K(T)ds + F_a\big(y_0\big)\right). \tag{4.16}$$

The additive kinetic functions can describe most of the transformation processes. Note that in many cases, $K(T)$, is in fact, the Arrhenius formula [67] expressing the temperature dependence of the rate of the process.

## 4.3 A Model for Non-Isothermal Oxidation

Starting from the isothermal kinetic function (4.2), the corresponding generalized kinetic function of the type in (4.16) can be constructed (see Appendix A). Let $y = x_{ox}(t)$, then $F_a(y) = y^2$, and substitute $K(T)$ for the Arrhenius equation (4.3). Then we have:

$$\frac{\partial F_a(y)}{\partial t} = \frac{\partial F_a(y)}{\partial T} = \frac{\partial K(\overline{T})}{\partial t} = 0,$$

and now we construct the generalized kinetic function:

$$\begin{aligned} &x_{ox} : \mathbb{R}_+ \longrightarrow \mathbb{R}_+, \\ &x_{ox}(t) = \left(k_0 \int_{t_0}^{t} \exp\left(-E_a/RT(s)\right) ds + x_{ox_0}^2\right)^{1/2}. \end{aligned} \tag{4.17}$$

that extends the isothermal oxidation model to the non-isothermal instance.

The industrial annealing process is typically carried out in at least three steps: heating, holding, and cooling (see Figure 4.1).
In this case, the temperature function $T(t)$ in (4.17) splits into three different subfunctions, depending on the domain where it stands. It can be represented in the piecewise defined function:

$$T(t) = \begin{cases} T_h(t) \ , \ t \in [0, t_1] \\ T_f \quad\ , \ t \in [t_1, t_2] \\ T_c(t) \ , \ t \in [t_2, t_3], \end{cases} \tag{4.18}$$

where $T_h(t) \in C'[t_1, t_2]$ represents the heating curve on the heating stage A→B, $T_f \in \mathbb{R}_+$ the temperature that is reached at the holding stage B→C, and $T_c(t) \in C'[t_1, t_2]$ the

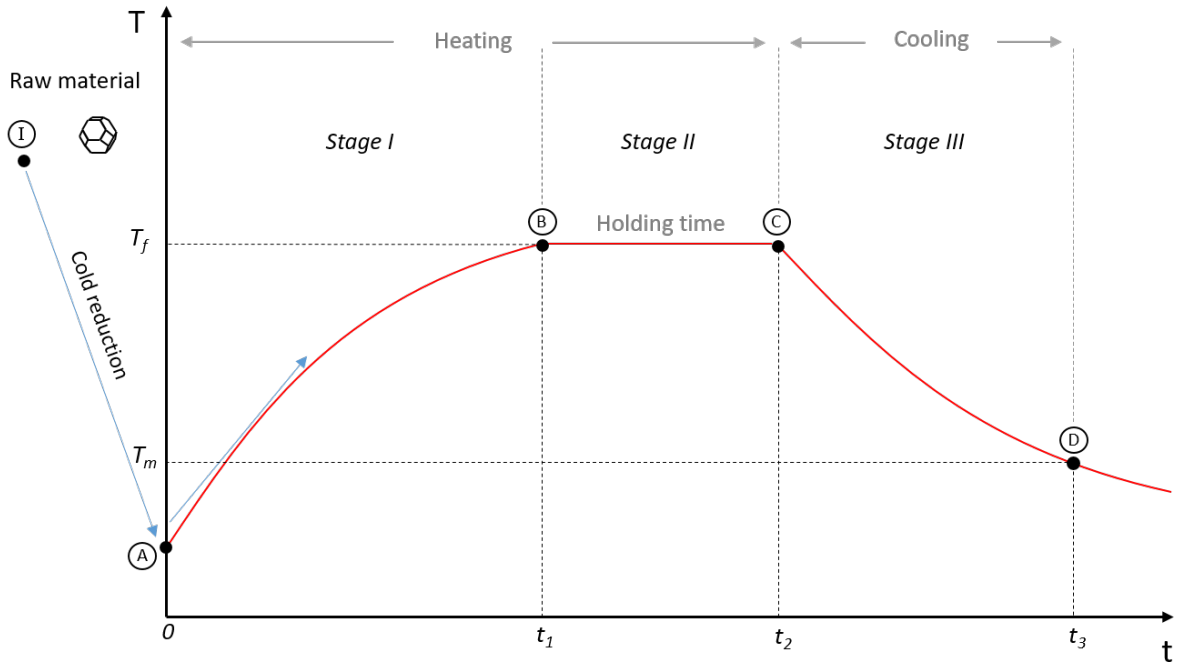


**Figure 4.1.** Different stages that can be part of the annealing process.

cooling curve on the cooling stage C→D.

Based on the above, and considering (4.1), (4.3), (4.17), and (4.18), for $J = 1, 2, 3$ corresponding to the alluded-to stages in the respective order, the net oxide-scale layer would be given by:

$$x_{ox}(t)_{NET} = \left( \sum_{j \in J} x_{ox}^2(t)_j \right)^{1/2} . \tag{4.19}$$

In this case, we have that $x_{ox_0} = 0$ at the first stage, since after the drawing process, the wire coils stay rust-free, then after subsequent stages, $x_{ox_0}$ becomes the previous scale thickness formation value.

The $k_0$ coefficient (the Arrhenius equation coefficient) represents the frequency of collision of the molecules. We gathered the value of $k_0$ to utilize in our model from [61] (see Appendix C). However, they calculated this constant from an experimental test performed isothermally. On the other hand, the bell-type furnace operation condition is far from operating fully isothermally. In this scenario, there is just one isothermal stage and two non-isothermal stages: heating and cooling. We hypothesize that the collision frequency of the molecules in the heating and cooling stages comes, to a lesser degree,

from the ones that take place on the holding stage and that the constant value for these stages should be a multiple of $k_0$. At the same time, activation energy ($E_a$) remains the same for the chemical components. Due to the just-exposed arguments, we propose to include $k_*$, another collision frequency parameter, in our mathematical model, to be used in the non-isothermal terms. This parameter is calculated in Appendix B based upon a scheme just developed in Section 4.5.

Substituting (4.17), (4.18), and (4.19), and considering all the above, we get to the following piecewise defined function:

$$x_{ox}(t)_{NET}=\begin{cases} \left\{k_* \int_0^t \exp\left(-E_a/RT_h(s)\right) ds\right\}^{1/2} & , t \in [0, t_1] \\ \left\{k_* \int_0^{t_1} \exp\left(-E_a/RT_h(s)\right) ds + k_0 \exp\left(-E_a/RT_f\right)(t-t_1)\right\}^{1/2} & , t \in [t_1, t_2] \\ \left\{k_* \int_0^{t_1} \exp\left(-E_a/RT_h(s)\right) ds + k_0 \exp\left(-E_a/RT_f\right)(t_2-t_1) + \right. & \\ \left. k_* \int_{t_2}^t \exp\left(-E_a/RT_c(s)\right) ds\right\}^{1/2} & , t \in [t_2, t_3]\,. \end{cases} \tag{4.20}$$

In (4.20), $k_0$, $E_a$ and $R$ are as defined above. 0 and $t_1$ represent the start and end times of the heating stage A→B , $(t_2 - t_1)$ the holding time, $t_2$ and $t_3$ the start and end times of the cooling stage C→D, and $k_*$ the newly proposed constant.

In order for our model to be usable, as mentioned above, we get the parameters $k_0$ (collision frequency) and $E_a$ (activation energy) from [61], since they performed several isothermal tests with very similar material and atmosphere conditions. We use $k_0$ in the isothermal terms of our model, while $k_*$ in the non-isothermal ones.

From (4.20) and with the Pilling-Bedworth ratio, we can determine the amount of metal that has been worn out by the oxide formation; the generalized kinetic function of the type in (4.16) for (4.7) would be:

$$x_{metal}(t) = \frac{1}{[PB]} x_{ox}(t)_{NET}. \tag{4.21}$$

With (4.20) and (4.21), it is possible to calculate the total scale after the annealing process and the total depth of the consumed metal, respectively. Although we study

three process stages, the analysis is not limited to these; a reader can extend it to further stages.

## 4.4 Change of the Wire Cross-Sectional Area

During the annealing process, a change in the wire cross-section area occurs because of the oxidation that takes place on the wire surface. On the one hand, we have the scale layer that crops up around the wire, and on the other, the reduction of the metal thickness due to the proper scale formation.

To represent this process, let $x'_{ox}(t)$ be the derivative of $x_{ox}(t)$ in equation (4.17) Section 4.1, $x'_{metal}(t)$ be the derivative of $x_{metal}(t)$ in (4.21), let $r$ be the wire radius and $A$ the wire cross-section area that changes along the time $t$. Then the following differential equation system can be established:

$$\frac{dr}{dt} = x'_{ox}(t) - x'_{metal}(t) = x'_{ox}(t)\left(1 - \frac{1}{[PB]}\right) \tag{4.22}$$

$$\frac{dA}{dr} = 2\pi r, \tag{4.23}$$

where $[PB]$ denotes the Pilling-Bedworth ratio (4.5). Solving for $r$ from equation (4.22) we have the following equations:

$$\begin{aligned} \int_{r_0}^{r} d\tilde{r} &= \int_0^t \left(1 - \frac{1}{[PB]}\right) x_{ox}(s)'ds \\ \implies r &= r_0 + \left(1 - \frac{1}{[PB]}\right) x_{ox}(t). \end{aligned} \tag{4.24}$$

Likewise, after rearranging equation (4.23) and substituting the result from (4.24), the following will be obtained:

$$\begin{aligned} &\frac{dA}{dr}\left(\frac{dr}{dt}\right) = 2\pi r\left(\frac{dr}{dt}\right) \\ &= 2\pi\left[r_0 + \left(1 - \frac{1}{[PB]}\right) x_{ox}(t)\right]\left(1 - \frac{1}{[PB]}\right) x'_{ox}(t). \end{aligned} \tag{4.25}$$

After substituting $x_{ox}(t)$ from (4.17) Section 4.1, in (4.25) in order to integrate it, we could integrate on both sides and solve for $A$:

$$A(t) = A_0 + 2\pi r_0\left(1 - \frac{1}{[PB]}\right)\sqrt{k_0}\left(\int_0^t \exp\left(-\frac{E_a}{RT(s)}\right) ds\right)^{0.5} + \int_0^t 2\pi\left(1 - \frac{1}{[PB]}\right)^2 \cdot \left[x_{ox_0} + \sqrt{k_0}\left(\int_0^t \exp\left(-\frac{E_a}{RT(s)}\right) ds\right)^{0.5}\right] \cdot \left[\frac{0.5\sqrt{k_0}\exp\left(-\frac{E_a}{RT(s)}\right)}{\left(\int_0^t \exp\left(-\frac{E_a}{RT(s)} ds\right)^{0.5}\right)}\right] ds,$$

after integration, $x_{ox_0}$ represents the initial scale layer (and the additional terms above are as defined in section 3.1).

After the cold-reduction process, a thin lubricant layer remains in the surface wire coils. As a consequence of the aforementioned, the wire surface remains rust-free for a while; then it is valid to consider $x_{ox}(0) = 0$:

$$A(t) = A_0 + 2\pi r_0\left(1 - \frac{1}{[PB]}\right)\sqrt{k_0}\left(\int_0^t \exp\left(-\frac{E_a}{RT(s)}\right) ds\right)^{0.5} + \pi\left(1 - \frac{1}{[PB]}\right)^2 \underbrace{\sqrt{k_0}\int_0^t \exp\left(-\frac{E_a}{RT(s)}\right) ds}_{\frac{x_{ox}(t)^2}{\sqrt{k_0}}}. \tag{4.26}$$

Substituting back $x_{ox}(t)$ from (4.17) for simplification in (4.26) and rearranging it becomes:

$$A(t) = A_0 + \pi\left(1 - \frac{1}{[PB]}\right) x_{ox}(t)\left[2r_0 + \frac{\left(1 - \frac{1}{[PB]}\right)}{\sqrt{k_0}} x_{ox}(t)\right]. \tag{4.27}$$

In (4.27), $x_{ox}(t)$ can be replaced by $x_{ox}(t)_{NET}$ from (4.20) to include the three process stages. The above result provides the wire cross-section area at time $t$ through the grown scale layer (considering that surface metal is worn out by the rise of the scale layer).

## 4.5 Parameter Calculation $k_*$

In Section 4.3, we raised the sought mathematical model to describe the non-isothermal oxidation formation outside the steel wire coils. That section introduced the $k_*$ parameter, proposed as an extra parameter specifically to the non-isothermal terms of

the model. In this section, the proposed $k_*$ parameter is calculated.

For $\mathscr{J} = 1, 2, ..., m$ number of experimental tests (see Chapter 5), consider the collection of temperature functions $\{T_j(t)\}_{j\in\mathscr{J}} \in C'[t_1, t_2]$, where for each $j \in \mathscr{J}$, $T_j(t)$ is defined in (4.18) in Section 4.3. For $\mathscr{K} = 1, 2, 3$, different thermal stages (according to Figure 4.1), consider the collection of time values $\cup_{j\in\mathscr{J}} \left\{t_k^j\right\}_{k\in\mathscr{K}}$ for the $m$ experimental tests. Now let $\psi_j(t) = \exp\left(-E_a/RT_j(t)\right)$, and regard the measured quantity collections of scale values $\left\{x_{ox_j}\right\}_{j\in\mathscr{J}} \in \mathbb{R}_+$ from the $m$ experiments.

After evaluating and squaring both sides of (4.20), the resulting equation for each $j \in \mathscr{J}$ and $k \in \mathscr{K}$ for the above-defined collections, it would yield:

$$\begin{aligned}
(x_{ox_1})^2 - k_0\psi_1(t)\Big|_{t_1^1}^{t_2^1} &= k_* \left(\int_0^{t_1^1} \psi_1(t)dt + \int_{t_2^1}^{t_3^1} \psi_1(t)dt\right) \\
(x_{ox_2})^2 - k_0\psi_2(t)\Big|_{t_1^2}^{t_2^2} &= k_* \left(\int_0^{t_1^2} \psi_2(t)dt + \int_{t_2^2}^{t_3^2} \psi_2(t)dt\right) \\
\vdots \qquad\qquad & \qquad\qquad \vdots \qquad\qquad \vdots \\
(x_{ox_m})^2 - k_0\psi_1(t)\Big|_{t_1^m}^{t_2^m} &= k_* \left(\int_0^{t_1^m} \psi_n(t)dt + \int_{t_2^m}^{t_3^m} \psi_m(t)dt\right).
\end{aligned} \tag{4.28}$$

If $k_*$ is treated as a unidimensional vector $\vec{k}_*$, then we may represent (4.28) by the linear system $A\vec{k}_* - Y = 0$, with $m$ equations and just one unknown variable. Nonetheless, we cannot directly solve for $\vec{k}_*$. In order to know its value, it is necessary to take a different approach.

Let $A, Y \in \mathbb{R}^{m\times n}$ be the associated matrix to the system, defined as:

$$A = \begin{bmatrix} \int_0^{t_1^1} \psi_1(t)dt + \int_{t_2^1}^{t_3^1} \psi_1(t)dt \\ \int_0^{t_1^2} \psi_2(t)dt + \int_{t_2^2}^{t_3^2} \psi_2(t)dt \\ \vdots \qquad\qquad \vdots \\ \int_0^{t_1^m} \psi_m(t)dt + \int_{t_2^m}^{t_3^m} \psi_m(t)dt \end{bmatrix} \; ; \; Y = \begin{bmatrix} (x_{ox_1})^2 - k_0\psi_1(t)\Big|_{t_1^1}^{t_2^1} \\ (x_{ox_2})^2 - k_0\psi_2(t)\Big|_{t_1^2}^{t_2^2} \\ \vdots \qquad\qquad \vdots \\ (x_{ox_m})^2 - k_0\psi_1(t)\Big|_{t_1^m}^{t_2^n} \end{bmatrix}$$

Along with the above system, we have a noise vector $e$ (instrumental noise likely) that comes from several measurements of sample 6 (see Section 5.1) on the same point. In the first instance, we could resort to the least squares method. However, this could raise the question: What if the resulting adjustment satisfies the data more accurately than

up to the noise level?. For if it were, we would fit the solution to the noise [42]. To address the problem, we will start by utilizing the Moore-Penrose pseudoinverse.

Let $A^\dagger$ be an $n \times m$ matrix over $\mathbb{R}$ of rank $r$ with nonzero singular values $\sigma_1 \geq \sigma_2 \geq \cdots \sigma_r$ and with the following properties:

$$\begin{aligned} AA^\dagger A &= A, \\ A^\dagger AA^\dagger &= A^\dagger, \\ \left(AA^\dagger\right)^* &= AA^\dagger, \\ \left(A^\dagger A\right)^* &= A^\dagger A. \end{aligned}$$

So, $A^\dagger$ is the Moore-Penrose pseudoinverse [35]. Then if $A = U\Sigma V^*$ is the SVD decomposition of $A$, the pseudoinverse $A^\dagger$ can be found by

$$A^\dagger = V\Sigma^\dagger U^*,$$

where $\Sigma^\dagger$ is defined by

$$\Sigma^\dagger_{ij} = \begin{cases} \frac{1}{\sigma_i} & \text{if } i = j \leq r \\ 0 & \text{anything else.} \end{cases}$$

Then, we could make

$$A^\dagger A\vec{k}_* \approx I\vec{k}_*,$$

from where we could find the $\vec{k}_*$ value. Another approach is to use a regularization method such as the Tikhonov regularization.

Let $\alpha > 0$ be a constant, the Tikhonov regularized [42] solution $\vec{k}_{*\,\alpha} \in \mathbb{R}$ to the system $A\,\vec{k}_* = Y$, is the minimizer:

$$\arg\min_{\vec{k}_*} F_\alpha(\vec{k}_*) = \frac{1}{2}||A\vec{k}_* - Y||^2 + \frac{\alpha}{2}||\vec{k}_*||^2, \tag{4.29}$$

where $\alpha$ is the regularization parameter. Such minimizer exists, and is found by:

$$\nabla F_\alpha(\vec{k}_*) = 0. \tag{4.30}$$

This way, from (4.30), it would be attained:

$$\begin{aligned}
0 =& \nabla F_\alpha(\vec{k}_*), \\
& \frac{1}{2}\sum_{i=1}^{n}\frac{\partial}{\partial\vec{k}_*}\left(\left(\sum_{j=1}^{n}A_{ij}\vec{k}_* - Y_i\right)\right)^2 + \frac{\alpha}{2}\sum_{j=1}^{n}\frac{\partial}{\partial\vec{k}_*}\vec{k}_*^2 \\
& = \frac{1}{2}\sum_{i=1}^{n}2\left(\left(\sum_{j=1}^{n}A_{ij}\vec{k}_*\right) - Y_i\right)(A_i) + \frac{\alpha}{2}(2\vec{k}_*) \\
& = \sum_{i=1}^{n}\left(\left(\sum_{j=1}^{n}A_{ij}\vec{k}_*\right) - Y_i\right)(A_i) + \alpha\vec{k}_* \\
& = (A\vec{k}_* - Y)A^* + \alpha I\vec{k}_* \\
& = A^*A\vec{k}_* - A^*Y + \alpha I\vec{k}_* \\
& = (A^*A + \alpha I)\vec{k}_* - A^*Y,
\end{aligned}$$

so, the solution to (4.29) is given by:

$$\vec{k}_* = (A^*A + \alpha I)^{-1}A^*Y, \tag{4.31}$$

where $A^*$ in this case is the transpose of $A$. This solution (4.31) is unique [43] (see Chapter 3 for a proof).

In order to find the solution (4.31), the regularization parameter $\alpha$ must be set. There are only a few methods to estimate the $\alpha$ value; one of them is the Morozov discrepancy principle, which is employed in this work. Assume that the data vector $Y$ is a noisy approximation of a noiseless vector $Y_0$ that is unknown to us. We may have an estimate of the noise level:

$$||Y - Y_0|| \simeq \epsilon,$$

for some $\epsilon > 0$. Let $\vec{k}_{*\,\alpha}$ be defined by (4.31), and set

$$f : \mathbb{R}_+ \longrightarrow \mathbb{R}_+ \ , \ \ f(\alpha) = ||A\vec{k}_{*\,\alpha} - Y||,$$

as the discrepancy function related to $\alpha$. The Morozov discrepancy principle [42] states that we cannot expect the approximate solution to yield a smaller residual error than the measurement error; the regularization parameter $\alpha$ should be chosen from the condition:

$$f(\alpha) = ||A\vec{k}_{*\,\alpha} - Y|| = \epsilon. \tag{4.32}$$

If possible, the regularized solution should not satisfy the data more accurately than up to the noise level. To set the noise level $\epsilon$ appearing in (4.32), we have to rely on a noise model. Consider the following formation model [33]:

$$Y = \underbrace{A\vec{k}_{*\,\alpha}}_{Y_0} + e,$$

when it is given:

$$e \in \mathbb{R}^m \sim \mathcal{N}(0,\, \sigma^2)$$

a random vector with independent components; this is the Gaussian additive noise model. Then, the following can be defined:

$$\epsilon^2 = E\left[||e||^2\right],$$

where $E$ is the expectation function [55] or mean, provided that for a random variable $X$, it is calculated by:

$$\mathrm{E}[X] = \int_{-\infty}^{\infty} x f_X(x) dx,$$

where $f_X(x)$ is the probability density function of $X$. In [42], they attain:

$$\begin{aligned} \epsilon^2 &= E\left[||e||^2\right] = N\sigma^2 \\ \implies \epsilon &= \sqrt{N}\sigma, \end{aligned} \tag{4.33}$$

provided that $N$ is the dimension of $A$, and that $\sigma$ [18] is given by:

$$\sigma = \sqrt{\int_{-\infty}^{\infty} (x - \mathrm{E}[X]^2)\, f_X(x) dx}.$$

With the aid of (4.33), we can determine a reasonable noise level $\epsilon$. This way, we can apply the Tikhonov regularization, along with the Morozov discrepancy principle, to obtain the $\vec{k}_*$ value. Appendix B, presents in detail how the value of the proposed $k_*$ in Section 4.3 was obtained.

# CHAPTER 5

# EXPERIMENTAL RESULTS

Chapter 4 raised a mathematical model targeted at predicting the scale layer thickness formation during the annealing process. In this chapter, we test the theoretical model accuracy against experimental data. To do so, some tests were performed in the actual process with different parameters. This chapter describes the experiments set up, the tested materials, and the established process parameters. Then, we present the experimental values obtained from the tests and the calculated values thrown by the model. Both data collections are compared against each other and their relation is displayed in a graph.

## 5.1 Experimental Procedure

A series of tests were performed on low-carbon steel wire drawing coils. All samples were 90% cold-reduced, starting from hot-rolled wire rod. The material was subjected to exothermic-oxidizing atmospheres [37]; we employed a bell-type furnace at full capacity material load for that end. For each run, we set different heating curves, temperatures, and annealing times. For some tests, the material cooled inside the furnace, while for others it was cooled at room temperature. At the end of each run, the batches were sampled, according to ASTM A853, taking complete spiral sections from the outside of the wire coils; then, the spirals were lab-tested. The details are summarized next.

**Table 5.1.** Properties of the steel used in each run.

| Id | AISI/SAE[54] | Chemical composition | | | | | | | | |
|---|---|---|---|---|---|---|---|---|---|---|
| # | Grade | C | Mn | Si | P | S | Cr | Mo | Ni | Cu |
| 1,2 | 1006 | 0.07 | 0.28 | 0.07 | 0.012 | 0.011 | 0.059 | 0.021 | 0.068 | 0.180 |
| 3 | 1006 | 0.07 | 0.29 | 0.08 | 0.004 | 0.006 | 0.017 | 0.004 | 0.014 | 0.015 |
| 4 | 1006 | 0.05 | 0.32 | 0.10 | 0.002 | 0.003 | 0.030 | 0.007 | 0.040 | 0.060 |
| 5,6 | 1006 | 0.05 | 0.28 | 0.07 | 0.012 | 0.010 | 0.079 | 0.021 | 0.070 | 0.190 |

In Table 5.1 the chemical compositions of the steel used in each run are shown; the values were determined by the ASTM E415 [13]. In Table 5.2, the furnace operational setups belonging to each run are shown. Heating and cooling curve functions are expressed in Kelvin, while the time variable $t$ is in seconds. A fitting from the furnace

**Table 5.2.** Furnace operational setup belonging to each run.

| Id | Feature | |
|---|---|---|
| # | $T_h(t) =$ | $T_c(t) =$ |
| 1 | $882 - 742 \cdot \exp(-t/8001) + 273$ | $265.431 + 522.101 \cdot \exp(-t/34635) + 273$ |
| 2 | $972 - 922 \cdot \exp(-t/18359) + 273$ | $-68 + 798 \cdot \exp(-t/53008) + 273$ |
| 3 | $924 - 720 \cdot \exp(-t/9690) + 273$ | $265.431 + 522.101 \cdot \exp(-t/34635) + 273$ |
| 4 | $32 + 0.222143t + 273$ | $14 + 784 \cdot \exp(-t/9978) + 273$ |
| 5 | $25 + 0.10t + 273$ | $92.5 + 697 \cdot \exp(-t/10597) + 273$ |
| 6 | $1188.67 - 770.171 \cdot \exp(-t/9153.38)$ | $265.431 + 522.101 \cdot \exp(-t/34635) + 273$ |

| Id | Feature | | | |
|---|---|---|---|---|
| # | Aust. temp $T_f$ $(K)$ | Heating time $(s)$ | Holding time $(s)$ | Cooling time $(s)$ |
| 1 | 1073 | 17625 | 0 | 59400 |
| 2 | 1003 | 24556 | 0 | 13545 |
| 3 | 1073 | 17045 | 2700 | 59400 |
| 4 | 1073 | 3458 | 190 | 3795 |
| 5 | 1063 | 7649 | 300 | 4450 |
| 6 | 1073 | 17100 | 1500 | 59400 |

atmosphere temperature and operating time generated the curves. These curves indeed are exponential functions, polynomials [29], or other real functions. Temperature data were acquired from a calibrated [40] k-type thermocouple settled inside the furnace; data were sampled each 30 min along the entire run. As Section 1 stated, it is assumed that the outer spiral wire coils possess the furnace atmosphere temperature all the time. Samples from Id run 1 to 3, and 6 cooled inside the furnace, while samples from Id run 4 and 5 cooled in steady air at $35°C$. The furnace atmosphere for all runs is composed of 1517 ppm V/V $CO_2$, 447 ppm V/V $O_2$, 14.7% V/V $O_2$. All tests were performed on a Nutec Bickley furnace.

All drawn wire samples were cold-reduced according to ASTM A853, A510 standards, from 5.5 mm-diameter wire rod. In all cases, wire rods were cold reduced to 1.75 +/- 0.05 mm diameter to produce the drawn wire samples. The depth of the scale was measured by metallography test, and sample preparation was performed by ASTM E3 [11] and ASTM E 407 [12] standards. Six samples were collected and measured from each run, and the average of the obtained results was reported.

## 5.2 Results and Discussion

Table 5.3 shows the experimentally obtained values and the calculated ones. The results agree with [67] in that the steel surface oxidized to a greater degree with higher annealing temperatures and longer annealing times.

| **Id #** | **Experimental $x_{ox}$ (mm)** | **Calculated $x_{ox}$ (mm)** |
|---|---|---|
| 1 | 0.0500 | 0.0508 |
| 2 | 0.0190 | 0.0168 |
| 3 | 0.0750 | 0.0800 |
| 4 | 0.0230 | 0.0250 |
| 5 | 0.0250 | 0.0270 |
| 6 | 0.0750 | 0.0670 |

**Table 5.3.** Experimentally measured and predicted values of scale thickness.

The reader can see that samples from Id 1, 3, and 6 exhibit a thicker oxide scale; this happened because these samples have the greatest annealing times and temperatures. The transformation of iron into oxide was also more significant in these samples than in their complement.

A maximum relative error of 11.5% is observed in the prediction of oxide-scale thickness. In Figure (5.1), the relationship between experimentally measured $x_{ox}$ calculations and predicted values using (4.20) for each run can be observed. The tests did not find decarburization on examined samples. According to [41], most steels having more than 0.30% C – this is in the AISI/SAE medium carbon steel range – are prone to surface carbon reduction to a greater or lesser degree. The chemical compositions of the steels studied in this work, detailed in Table 5.1, are far below this value, and this is also the case in the low carbon steel annealed wire process.

In Figure (5.2), the reader can see the metallographic test results performed at 1000X optical zoom, from which the scale depth ($x_{ox}$) was measured for each sample displayed in Table (5.3), from Id 1 to Id 6. This test was measured punctually over the worn-out surface, the whole oxide-scale thickness, along with the $\alpha_1$, $\alpha_2$, and $\alpha_3$ oxide sub-layers.

In general, the predicted results from the mathematical model raised in this document render with good accuracy the studied phenomenon that takes place in the annealing

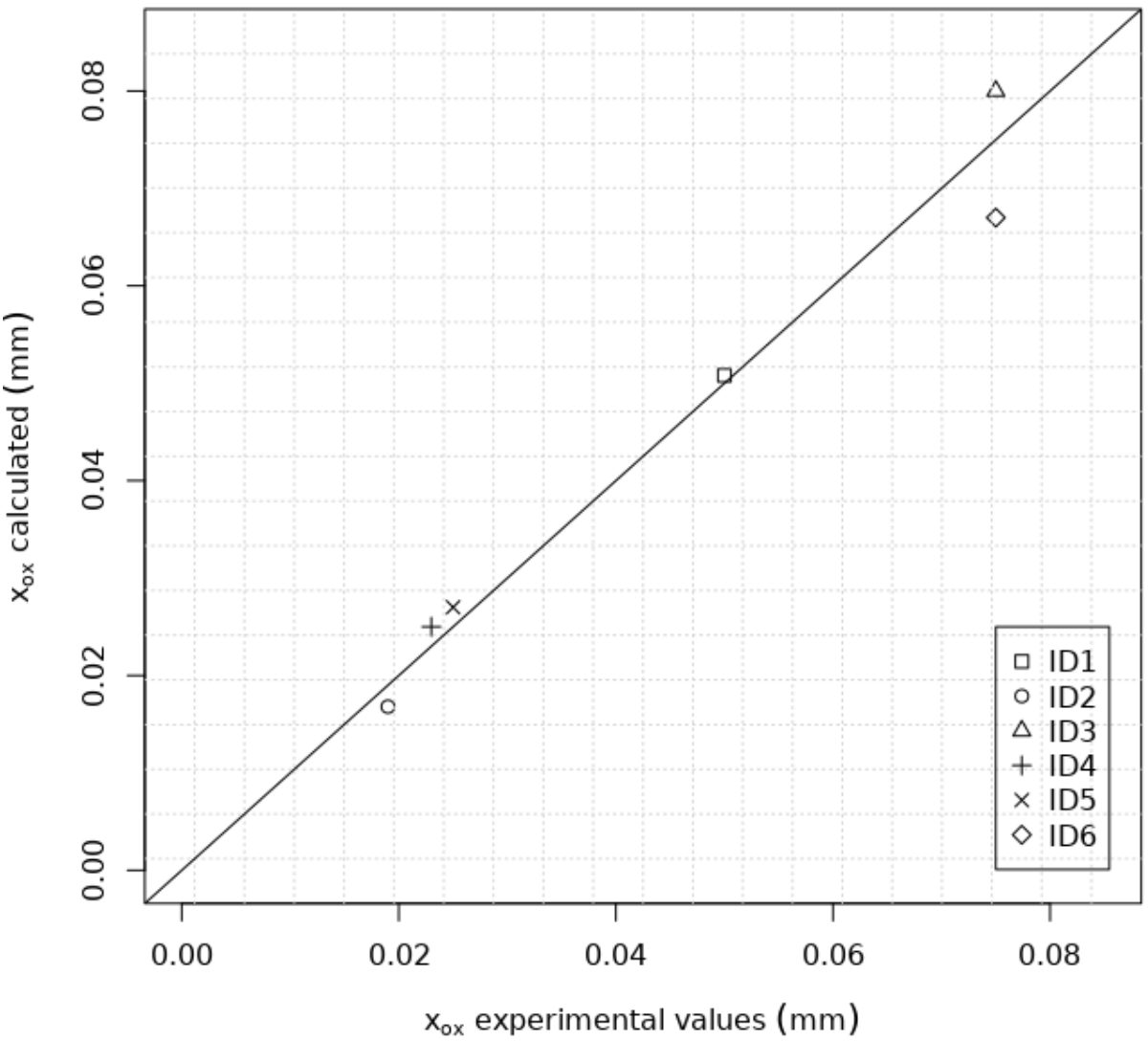


**Figure 5.1.** Relationship between the experimentally measured oxide-scale thickness values and the predicted by (4.20).

process. However, the reader can observe that most predicted values are below the experimentally obtained results. This discrepancy is mainly due to the approximation of the outside steel coil spiral temperature to the furnace atmosphere's (heating and cooling curves in Table 5.1) that was set in Section 4. Thus, by including a heat transfer model that properly describes the change in temperature of the steel coils in the furnace to obtain more accurate heating and cooling curves, more accuracy in the theoretically predicted results will be attained.

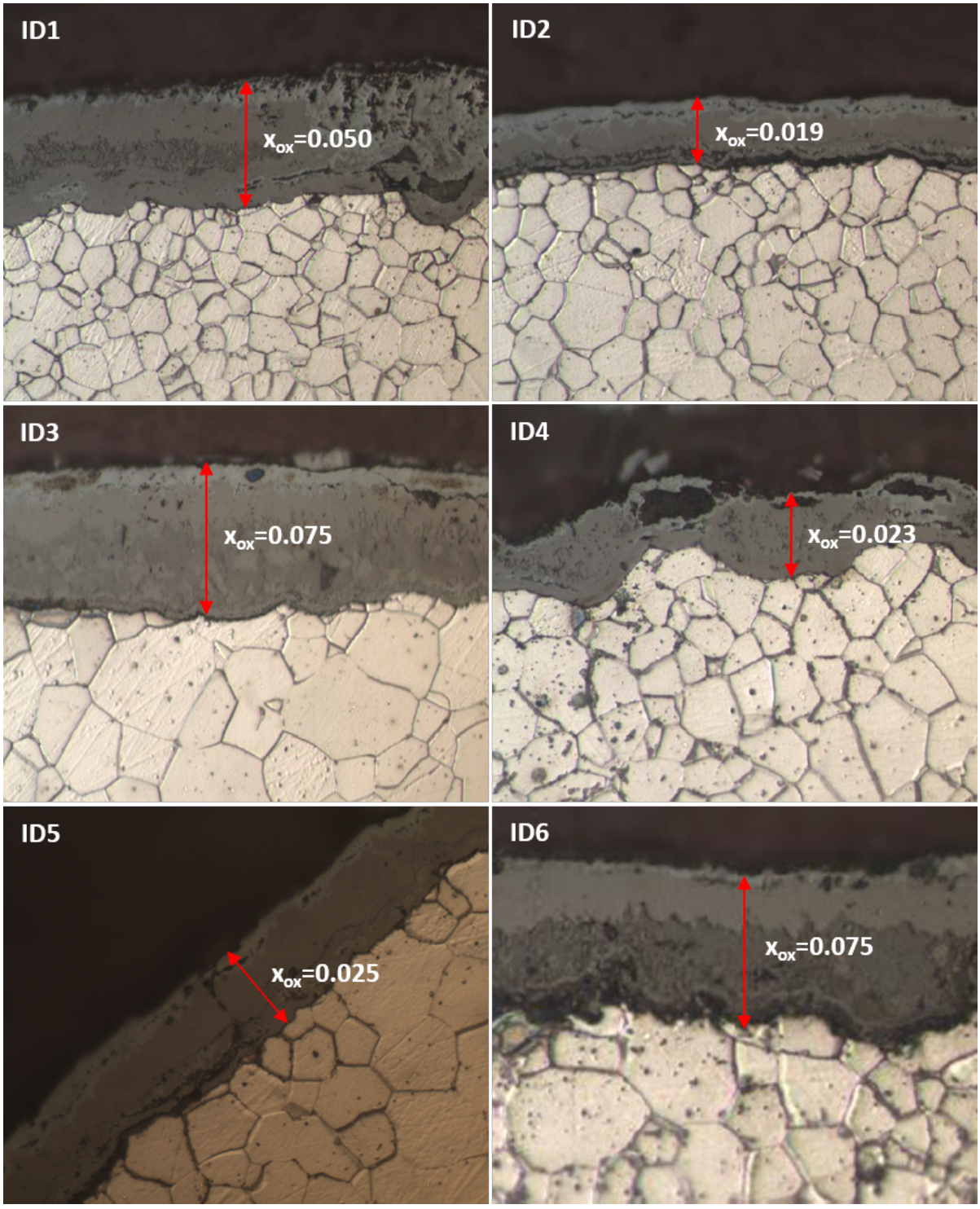


**Figure 5.2.** Metallographic scale depth measure results for each sample from Table 5.3, performed at 1000X. Values are reported in millimeters.

# CHAPTER 6
# CONCLUSIONS AND FUTURE WORK

## 6.1 Conclusions

A mathematical model was developed to describe the oxidation phenomenon in the material during the annealing process of hypoeutectoid steel cold-drawn wire. Six process runs were carried out and subjected to monitoring to verify the validity of the models. This model reproduced with reasonable accuracy the experimental results obtained from the measures on the samples since we got a maximum relative error of 11.5% in the prediction of oxide-scale thickness. On the other hand, it is worth mentioning that the approximation set in Section 4 – that the temperature of the outside of the drawn wire coils equals the furnace atmosphere's temperature – turned out to be a good approximation at predicting the experimental results that Section 5 revealed. This approximation restricts the predictability of the models only to the outer spirals of the annealed wire coils (Figure 1, Section 1). Actually, according to ASTM A853, this is the section from the samples that should be extracted to perform lab tests so that at this stage, the model was helpful for us, at least for quality control purposes.

We proposed adding an extra parameter $k_*$ in the non-isothermal stages of the model. The obtained value of this parameter supports our hypothesis that this parameter should be a fraction of the former [61]. Also, it is crucial to note that the results agreed with [67] because the steel surface oxidized to a greater degree with higher annealing temperatures and longer annealing times. To provide a proper full description of the temperature profile of the entire coil, a furnace heat transfer model would have to be considered to give off the corresponding heating and cooling curves. For if it were included, we would only need to input these curves into the model developed here, carrying out the calculations in the same way they were done in this document.

## 6.2 Future Work

In this work, we proposed a mathematical model to calculate the oxide-scale thickness of the outer spirals of the steel wire coils. The model can predict only in this section because we assumed that the temperature of the outside coils equals the furnace atmosphere, so that we have no information about the temperature behavior in the inner zones. At this stage, this work could be helpful to complement the quality control

tests in an industrial setup since these tests typically perform on the same outer section of the coils. Nevertheless, it is natural to ask now about the rest of the coil sections. A heat transfer model is just needed to attain that task to predict the scale formation over the inner area of the material.

To broaden the pertinence of this work, we set the development of a heat transfer model that describes the evolution of the temperature on the whole body of the drawn wire coils as possible future work. On the other hand, the inclusion of a heat transfer mechanism to the mathematical model raised in this work would significantly improve the accuracy of the scale thickness predicted values.

# APPENDIX A

# MATHEMATICAL TREATMENT FOR NON-ISOTHERMAL TRANSFORMATION EXAMPLES

# MATHEMATICAL TREATMENT FOR NON-ISOTHERMAL TRANSFORMATION EXAMPLES

This appendix presents a set of examples of the mathematical treatment for non-isothermal transformations [53], as detailed in Chapter 4. Recall that their purpose is to generalize the conventional isothermal kinetic functions that describe the thermally activated process into some new types of kinetic functions that are suitable for the phenomenological description of the non-isothermal process. This appendix also describes the transformation of equation (4.1) raised in Chapter 4.

## A.1 Example 1

As a first example, consider the following kinetic equation:

$$\left(\ln \frac{1}{1-y}\right)^{1/m} - K(T)t = 0, \tag{A.1}$$

and proceed with the non-isothermal transformation.

The above equation has the shape of (4.10):

$$F_a(y) - K(T)t = 0.$$

then we start by constructing the generalized additive kinetic function in the form of equation (4.12):

$$y(t) = F_a^{-1}\left(\int_{t_0}^{t} K(T)ds + F_a\big(y_0\big)\right).$$

So, from (A.1) we construct the generalized additive kinetic function in the following way:

$$A := \int_{t_0}^{t} K(T)ds + \left(\ln \frac{1}{1-y_0}\right)^{1/m}. \tag{A.2}$$

Then we are going to look for an inverse or general inverse for (A.2), in terms of $Fa(y)$. It is held from (A.2) that:

$$F_a(y) = \left(\ln \frac{1}{1-y}\right)^{1/m}, \tag{A.3}$$

Now we continue with the transformation by applying an inverse or inverses to (A.3), to solve for $y$. Then the same operation will be applied for $A$ from (A.2). This is

$$\begin{aligned}
&\left(\ln \frac{1}{1-y}\right)^{1/m} && A = \int_{t_0}^{t} K(T)ds + \left(\ln \frac{1}{1-y_0}\right)^{1/m} \\
&\ln \frac{1}{1-y} && A^m \\
&\frac{1}{1-y} && \exp(A^m) \\
&1-y && \exp(A^m)^{-1} \\
&-y && -1 + \exp(A^m)^{-1} \\
&y && 1 - \exp(A^m)^{-1}.
\end{aligned}$$

$$\implies y = 1 - \exp(A^m)^{-1} \tag{A.4}$$

Finally, we substitute $A$ from (A.2) in the last obtained equation (A.4), and simplify to obtain:

$$y(t) = 1 - \exp\left[\left(\int_{t_0}^{t} K(T)ds + \left(\ln \frac{1}{1-y_0}\right)^{1/m}\right)^{m}\right]^{-1}. \tag{A.5}$$

This is the generalized kinetic function for (A.1) that was sought. Now (A.6) can be used to describe the kinetics it describes, extended to the non-isothermal instance.

## A.2 Example 2

In completely martensitic quenched steel, the decrease of the Vickers hardness $H_v$, due to the tempering at a constant temperature, is characterized by the isothermal kinetic function [53]:

$$H_v(t) = H_{v_0} - B\left[\exp\left(\frac{-Q}{RT}\right)t\right]^{n}, \tag{A.6}$$

where $H_{v_0}$ represents the hardness of the martensite after quenching, and $B$, $n$, and $Q$ are empirical constants.

As a second example, apply the non-isothermal transformation to (A.6).

We start from (A.6), let $y = H_v(t)$ and $K(T) = \exp\left(\frac{Q}{RT}\right)$, then substitute in (A.6) and it becomes:

$$y = y_0 - B\left[K(T)t\right]^n. \tag{A.7}$$

Next, arrange (A.7) to end with an equation of the form (4.10):

$$\begin{aligned} y - y_0 &= B\left[K(T)t\right]^n \\ \left(\frac{y_0 - y}{B}\right)^{1/n} &- K(T) = 0, \end{aligned} \tag{A.8}$$

and we have $F_a(y) = \left(\frac{y_0 - y}{B}\right)^{1/n}$. Now transform (A.8) to the form of equation (4.12) in the following way:

$$\begin{aligned} &\left(\frac{y_0 - y}{B}\right)^{1/n} && A = \int_{t_0}^{t} K(T)ds + \left(\frac{y_0 - y_0}{B}\right)^{1/n} \\ &\frac{y_0 - y}{B} && A^n \\ &y_0 - y && BA^n \\ &\quad - y && -y_0 + BA^n \\ &\quad y && y_0 - BA^n. \end{aligned}$$

$$\implies \; y = y_0 - BA^n. \tag{A.9}$$

Substitute for $A$ in (A.9), and $y$ and $K(T)$ back, finally it would be obtained:

$$H_v(t) = H_{v_0} - B\left[\int_{t_0}^{t} \exp\left(\frac{-Q}{RT}\right) ds\right]^n. \tag{A.10}$$

Equation (A.10) represents the generalized kinetic equation of (A.6).

## A.3 Oxidation Equation

The mathematical treatment of the non-isothermal oxidation equation (4.20) will be described. Recall from Chapter 4 the oxidation equation:

$$x_{ox}^2(t) = k_0 exp(-E_a/RT)t. \tag{A.11}$$

Let $y = x_{ox}(t)$ and $K(T) = k_0 exp(-Ea/RT)$ and substitute them in (A.11). This way we would have the following expression:

$$y^2 = K(T)t, \tag{A.12}$$

so that $F_a(y) = y^2$. Now arrange (A.12) to end with an equation of the form (4.10):

$$y^2 - K(T)t = 0. \tag{A.13}$$

Next, transform (A.13) to the form of equation (4.12) in the following way:

$$\begin{array}{ll} y^2 & A = \displaystyle\int_{t_0}^{t} K(T)ds + y_0^2 \\ y & A^{1/2}. \end{array}$$

$$\Longrightarrow y = A^{1/2}. \tag{A.14}$$

Substitute for $A$ in (A.14), and $y$ and $K(T)$ back. Finally you will obtain:

$$\begin{aligned} y &= \left( \int_{t_0}^{t} K(T)ds + y_0^2 \right)^{1/2} \\ x_{ox}(t) &= \left( k_0 \int_{t_0}^{t} \exp(-E_a/RT)ds + x_{ox0}^2 \right)^{1/2}. \end{aligned} \tag{A.15}$$

Then (A.15) is the generalized kinetic equation of (A.11). This equation is (4.13), the one used in Chapter 4, Section 4.3 that extends the isothermal oxidation model to the non-isothermal instance.

# APPENDIX B

# NUMERICAL DETERMINATION OF THE PARAMETER $k_*$

# NUMERICAL DETERMINATION OF THE PARAMETER $k_*$

This appendix reveals the performed computations to achieve the determination of the $k_*$ parameter for the non-isothermal terms in equations (4.20) and (4.21), a parameter that was proposed in Chapter 4, Section 3.3. The calculations performed here are based on the theory developed in Section 3.4 from Chapter 4. We use both the Moore-Penrose pseudoinverse and the Tikhonov regularization. We have utilized the Python 3 programming language to carry out the actual computations.

We start by evaluating the matrices raised at the beginning of Section 3.3 from Chapter 4. To evaluate them, substitute the data contained in Table 5.2 from Section 5.1 in each entry and compute the integrals numerically. Then, substitute $x_{ox_j}$ values for each $j = 1, 2, ..., m$ experimental test:

$$A = \begin{bmatrix} \int_0^{t_1^1} \psi_1(t)dt + \int_{t_2^1}^{t_3^1} \psi_1(t)dt \\ \int_0^{t_1^2} \psi_2(t)dt + \int_{t_2^2}^{t_3^2} \psi_2(t)dt \\ \vdots \quad\quad\quad \vdots \\ \int_0^{t_1^m} \psi_m(t)dt + \int_{t_2^m}^{t_3^m} \psi_m(t) \end{bmatrix} = \begin{bmatrix} 4.762934e-11+3.022701e-11 \\ 4.236877e-12+4.23287e-12 \\ 4.101169e-11+3.022701e-11 \\ 2.872622e-12+7.904576e-12 \\ 4.617494e-12+7.254174e-12 \\ 3.627276e-11+3.022701e-11 \end{bmatrix}$$

$$Y = \begin{bmatrix} (x_{ox_1})^2 - k_0\psi_1(t)\big|_{t_1^1}^{t_2^1} \\ (x_{ox_2})^2 - k_0\psi_2(t)\big|_{t_1^2}^{t_2^2} \\ \vdots \quad\quad\quad\quad \vdots \\ (x_{ox_m})^2 - k_0\psi_1(t)\big|_{t_1^m}^{t_2^n} \end{bmatrix} = \begin{bmatrix} 0.0025-0 \\ 0.000361-0 \\ 0.005625-0.00414091 \\ 0.000529-0.0002913974 \\ 0.000625-0.0003419357 \\ 0.005625-0.002300506 \end{bmatrix}$$

To estimate the noise level, six measures were performed on the same point on the 0.0750 mm-scale thickness sample. From the obtained data, this vector was created:

$$e = [0, 8e-4, 0, 1e-4, 1.1e-3, 0]$$

that is the distance from the average to each value. Once we have gathered the above data, we can go on with the rest of the computations. Listing B.1 shows these computations.

```
##############################################################################################
###              Full set of instructions to determine k_* parameter                     ###
##############################################################################################

import numpy as np
import scipy.sparse as sp
import scipy.sparse.linalg as la
import matplotlib.pyplot as plt
from numpy import linalg as lg
from scipy.linalg import norm
from numpy import array
from sklearn.linear_model import Ridge
from sklearn.datasets import make_regression
import math

# We create the A matrix with the above-presented data.
A = np.array([[4.762934e-11 + 3.022701e-11],
[4.236877e-12 + 4.23287e-12],
[4.101169e-11 + 3.022701e-11],
[2.872622e-12 + 7.904576e-12],
[4.617494e-12 + 7.254174e-12],
[3.627276e-11 + 3.022701e-11]])

# Next, we create the solution vector with the same above presented data.
Y=np.array([[0.0025 - 0],
[0.000361 - 0],
[0.005625 - 0.00414091],
[0.000529 - 0.0002913974],
[0.000625 - 0.0003419357],
[0.005625 - 0.002300506]])

# Then our linear system is: Ak_* - Y = 0.
# We check the condition number of the matrix A:
lg.cond(A)
# Output: 1.0
# This means that at least the matrix is not badly conditioned.
# Let us start with the calculation of the Moore-Penrose pseudoinverse.

PINV_A=np.linalg.pinv(A,rcond=0)

# Determine the k_* value using the pseudoinverse.
k=PINV_A.dot(Y)
print(k)
# Output: 33385922.34941649

# Optional, verify the solution by the Moore-Penrose pseudoinverse.
print(Y)
A.dot(k)
plt.scatter(Y,Y,c='red')
plt.scatter(A.dot(k),Y,c='green')

# Now introduce the e vector data values to estimate the noise level.
# Truncate its value to 5 decimals after point.
e = [0, 8e-4, 0, 1e-4, 1.1e-3, 0]
```

```
epsilon = math.trunc(np.std(e) * math.sqrt(len(e)) * 100000) / 100000
print(epsilon)
# Output: 0.00141

# Propose several possible alpha values for the Tikhonov regularization.
alphas = [1e-26, 1e-25, 1e-24, 1e-23, 1e-22, 1e-21, 1e-20, 1e-19, 1e-18]

# Proceed to regularize the linear system {Ak_* - Y = 0}, by the use of the Tikhonov
    regularization.
norm_r = []
for alphaa in alphas:
    clf = Ridge(alpha=alphaa)
    clf.fit(A, Y)
    obt_val_01=clf.predict(A)
    Y_p = obt_val_01
    norm_r.append(norm(Y_p - Y,2))

# Now by the Morozov discrepancy principle, and the Moore-Penrose pseudoinverse, a
    suitable alpha
# parameter will be chosen.
# See above displayed figure.
plt.loglog(alphas, norm_r, "-ob", label="||A k - Y ||")
plt.loglog(alphas, [norm(A.dot(k)-Y,2)]*len(alphas), "-g", label="||A.dot(k)-Y||")
plt.loglog(alphas, [epsilon]*len(alphas), "-r", label="epsilon")
plt.xlabel("alpha")
plt.legend()
plt.title("Morozov discrepancy principle")
plt.show()

# By the above figure, it is resolved that the adequate alpha value according to the
    Morozov discrepancy principle,
# would be:
alfa = 1e-22

# Finally, we solve the linear system {Ak_* - Y = 0} for k_*, by the use of this alpha
    value.
clf = Ridge(alpha=alfa)
clf.fit(A, Y)
Y_final_value=clf.predict(A)

# Optional, verify the solution by the Tikhonov regularization.
print(Y)
print(Y_final_value)
plt.scatter(Y,Y,c='red')
plt.scatter(Y_final_value,Y,c='green')

# Obtain the actual k_* value.
k_ = clf.coef_
print(k_)
# Output: 33141806.49267787
```

**Listing B.1.** Determination of $k_*$ parameter.

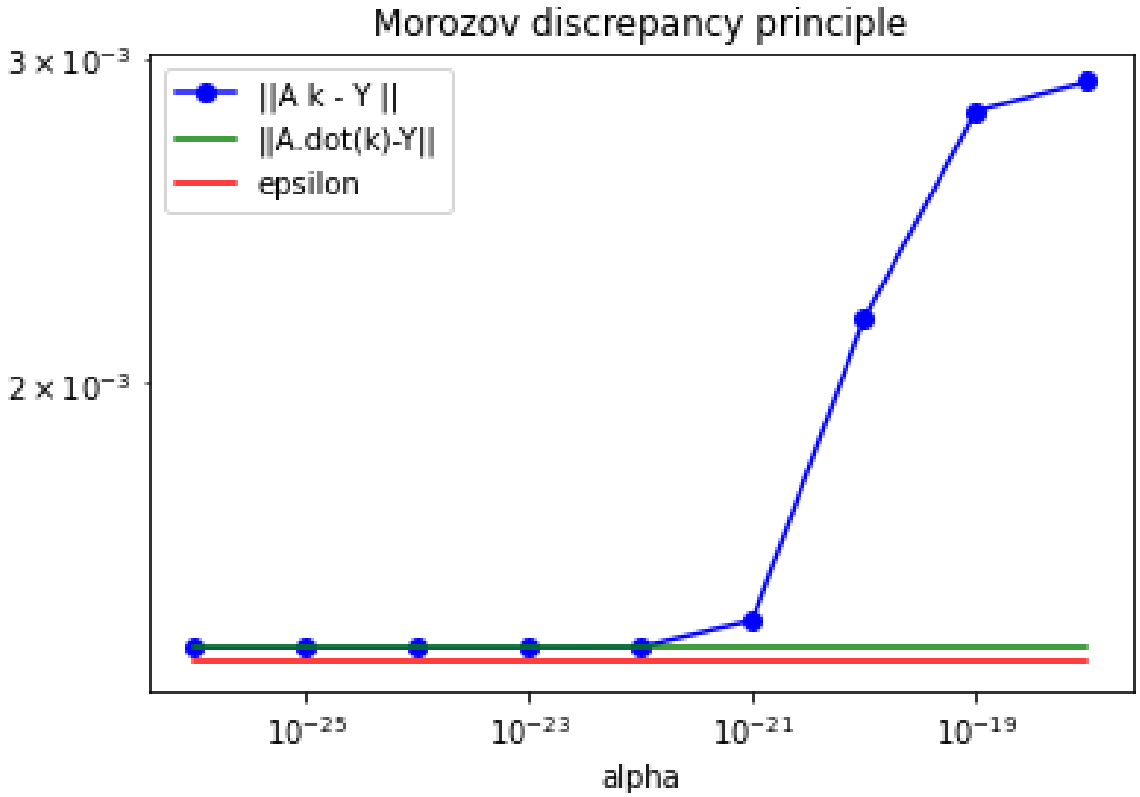


**Figure B.1.** The Moore-Penrose and Tikhonov regularization results.

Figure B.1 displays a plot from the results obtained by the Moore-Penrose results, the green line, and the Tikhonov regularization, the blue and red lines. By the Morozov discrepancy principle, we choose an $\alpha$ value of 1e-22. After solving the linear system for $k_*$ with the Tikhonov regularization with this $\alpha$ value, we obtain $k_* = 33141806$ for our proposed parameter, at least for the materials, temperature conditions, and temperature curves shown in Table 5.1, and Table 5.2 from Chapter 5. For those readers interested in inverse problems, some examples can be found in [39].

# APPENDIX C
# MODEL PARAMETERS SUMMARY

# MODEL PARAMETERS SUMMARY

## C.1 Model parameters

Chapter 4 raised the mathematical model to approach the studied phenomenon: oxidation. To make use of this model, parameters needed for it were gathered mainly from the bibliography. This section summarizes the required parameters; Table C.1 provides them next.

**Table C.1.** Oxidation model parameters.

| **Parameter** | **Value** | **Ref.** |
|---|---|---|
| $k_0$ | 77400000 | [61] |
| $Ea$ | 281476 $J/mol$ | [61] |
| $k_*$ | 33141806 | Appendix B |
| $R$ | 8.314 $J \cdot mol^{-1}K^{-1}$ | [56],[57] |
| $\alpha_1$ | 0.95 | [61],[67] |
| $\alpha_2$ | 0.04 | [61],[67] |
| $\alpha_3$ | 0.01 | [61],[67] |
| $\beta_1$ | 1.75 | [67],[28] |
| $\beta_2$ | 2.10 | [67],[28] |
| $\beta_3$ | 2.14 | [67],[28] |

Note: Original values for $k_0$ and $Ea$ from [61] are 8.8x10$^6$ and 140738 J/mol, respectively, for temperatures $T < 1173$K whose mathematical model is $x[\mu m] = K \cdot \sqrt{t}$. These values were converted to be usable for the isothermal model $x^2[mm] = K \cdot t$, which our model is based on.

# GLOSSARY

**AISI** American Iron and Steel Institute. vi, 11, 49, 51, 68

**ASTM** American Society for Testing and Materials. vi, 1, 14, 49, 50, 54, 68

**IEC** Institute of Electronics and Computer. 68, 75

**ISO** International Organization for Standarization. 68, 75

**SAE** Society of Automotive Engineers. vi, 12, 49, 51, 68, 70

# LIST OF TABLES

# LIST OF FIGURES

PAGE

# AUTOBIOGRAFÍA

**José Alfredo Sánchez de León**
Candidato para el Grado de Maestría en Ciencias
con Orientación en Matemáticas
Universidad Autónoma de Nuevo León
Facultad de Ciencias Físico Matemáticas

Tesis:
A Mathematical Model for the Prediction of the
Scale Layer Formation on ASTM A510/A853 Cold-Drawn
Hypoeutectoid Steel Wire After Batch Annealing

Es ingeniero químico egresado de la Facultad de Ciencias Químicas de la Universidad Autónoma de Nuevo León. Ha estado laborando para Grupo Villacero durante más de 13 años, actualmente se desempeña como gerente de calidad en la Planta Trefilados D. D.

Se describen a continuación las publicaciones y actividades realizadas durante el período de estudios de posgrado.

Capítulos de libro:

1. de León, J. A. S. *Alternative Representation for Binomials and Multinomies and Coefficient Calculation*, Mathematical Theorems - Boundary Value Problems and Approximations, Lyudmila Alexeyeva, IntechOpen, 99-115 (2020) DOI: 10.5772/intechopen.91422.

Artículos:

1. de León, J.A.S. *Calculation of Binomial and Multinomial Coefficients by Sequences of Summations*. Math.Comput.Sci. 13, 403–415 (2019). DOI: 10.1007/s11786-019-00403-w.

2. de León, J.A.S. *A Model for Calculation of a Productivity Bonus*. Eureka, 42, 10-27 (2018). https://www.uaq.mx/ingenieria/publicaciones/eure-uaq/n42/sanchez.pdf

Conferencias impartidas:

1. *Calculation of Binomial and Multinomial Coefficients by Sequences of Summations.* LII Congreso de la Sociedad Matemática Mexicana, Universidad Autónoma de Nuevo León (21 al 25 de octubre 2019), San Nicolás de los Garza, N. L.

2. *Formulación Matemática de Ecuaciones de Dimensionamiento de Costura de Tubería Helicoidal* (modalidad de póster). LII Congreso de la Sociedad Matemática Mexicana, Universidad Autónoma de Nuevo León (21 al 25 de octubre 2019), San Nicolás de los Garza, N. L.

3. *Parameters Calculation for Eddy Currents Device* (presentación de proyecto). 2o Workshop-Coloquio Industria 4.0. Universidad Autónoma de Nuevo León (01 al 02 de noviembre 2018), San Nicolás de los Garza, N. L.

4. *Desarrollo de Estructura Metálica Sustentable para Carga* (presentación de proyecto). XXV Congreso Internacional sobre Ciencia y Tecnología. Universidad Autónoma de Nuevo León (20 al 28 de octubre 2018), San Nicolás de los Garza, N. L.

5. *Concatenation Operator for Piecewise-defined Functions* (modalidad de póster). 6th European Seminar on Computing (ESCO 2018), (3 al 8 de junio 2018), Pilsen, República Checa.

# BIBLIOGRAPHY


[1] *29 - heat treatment*, in Smithells Metals Reference Book (Eighth Edition), W. Gale and T. Totemeier, eds., Butterworth-Heinemann, Oxford, eighth edition ed., 2004, pp. 29–1–29–83.

[2] H. T. Abuluwefa, R. I. L. Guthrie, and F. Ajersch, *Oxidation of low carbon steel in multicomponent gases: Part ii. reaction mechanisms during reheating*, Metallurgical and Materials Transactions A, 28A (199y), pp. 1643–1652.

[3] Y. Al-Zain, *Properties of engineering materials the structure of crystalline solids.* http://kaizenha.com/wp-content/uploads/2018/01/Dr.-Yazan-Al-Zain-Ch.-3-2.pdf, 2018. Accessed: 2021-05-15.

[4] V. Albani, A. De Cezaro, and J. P. Zubelli, *On the choice of the tikhonov regularization parameter and the discretization level: A discrepancy-based strategy*, Inverse Probl. Imaging, 10 (2016), pp. 1–25.

[5] A. Aran, *Metallography.* https://web.itu.edu.tr/~arana/macro-micro.pdf, 2006. Accessed: 2021-05-15.

[6] S. A. Ashter, *Mechanics of Materials. Thermoforming of Single and Multilayer Laminates, 123–145*, Elsevier, United States, 2014.

[7] ASTM A370 - 20. *Standard test methods and definitions for mechanical testing of steel products.*, standard, American Society for Testing and Materials, Philadelphia, USA, Sept. 2020.

[8] ASTM A510/A510M - 11. *Standard specification for general requirements for wire rods and coarse round wire, carbon steel, and alloy steel*, standard, American Society for Testing and Materials, Pennsylvania, USA, Jan. 2011.

[9] ASTM A853 - 04 (Reapproved 2010). *Standard specification for steel wire, carbon, for general use*, standard, American Society for Testing and Materials, Philadelphia, USA, Apr. 2010.

[10] ASTM E112 - 13. *Standard test methods for determining average grain size.*, standard, American Society for Testing and Materials, Pennsylvania, USA, Aug. 2014.

[11] ASTM E3 - 11. *Standard guide for preparation of metallographic specimens.*, standard, American Society for Testing and Materials, Philadelphia, USA, June 2017.

[12] ASTM E407 - 07. *Standard practice for microetching metals and alloys.*, standard, American Society for Testing and Materials, Pennsylvania, USA, May 2007.

[13] ASTM E415 - 17. *Standard test method for analysis of carbon and low-alloy steel by spark atomic emission spectrometry.*, standard, American Society for Testing and Materials, Pennsylvania, USA, Aug. 2017.

[14] ASTM E7 - 03. *Standard terminology relating to metallography*, standard, American Society for Testing and Materials, Pennsylvania, USA, 2003.

[15] ASTM E8/E8M - 16a. *Standard test methods for tension testing of metallic materials.*, standard, American Society for Testing and Materials, Philadelphia, USA, Aug. 2020.

[16] J. M. Atienza, *Tensiones Residuales en Alambres de Acero Trefilados*, PhD thesis, Universidad Politécnica de Madrid, Madrid, SP, 2001.

[17] P. Atkins and J. de Paula, *Atkin's Physical Chemistry*, W. H. Freeman and Company, NY, USA, 2006.

[18] D. P. Bertsekas and J. N. Tsitsiklis, *Introduction to Probability*, Massachusetts Institute of Technology, MA USA, 2000.

[19] W. E. Boyce and R. C. DiPrima, *Ecuaciones Diferenciales y Problemas con Valores en la Frontera 4a Ed.*, Editorial Limusa, México, 2000.

[20] G. S. Brady, H. R. Clauser, and V. J. A., *Materials Handbook 15th Ed.*, McGraw-Hill, USA, 2002.

[21] Cabrera and Mott, *Parabolic law - an overview*, in Physical Metallurgy (4th Ed.), R. W. Cahn and P. Haasen, eds., vol. 2, Elsevier, Holland, 1996, pp. 1291–1361.

[22] W. D. Callister and D. G. Rethwisch, *Materials Science and Engineering An Introduction*, Wiley, Hoboken, NJ, 2010.

[23] G. W. Castellan, *Fisicoquímica Segunda Edición*, Addison Wesley Longman, NY USA, 1987.

[24] M. L. Castro and Fornaro, *Microscopy in the study of metallic alloys*, Acta Microscopica, 19(1) (2010), pp. 94–99.

[25] J. Cengel and M. Boles, *Thermodynamics An Engineering Approach Eighth Edition*, McGraw-Hill, NY USA, 2014.

[26] R. Chang, *Chemistry 10th Ed.*, McGraw-Hill, NY, USA, 2010.

[27] E. A. Coddington, *An Introduction to Ordinary Differential Equations*, Dover Publications, NY, USA, 1989.

[28] B. C. De Cooman and J. G. Speer, *Fundamentals of Steel Product Physical Metallurgy (AIST)*, ASM International, PA, USA, 2011.

[29] J. A. S. de León, *Alternative representation for binomials and multinomies and coefficient calculation*, in Mathematical Theorems - Boundary Value Problems and Approximations, L. Alexeyeva, ed., vol. 1, IntechOpen, London, UK, 2020, pp. 99–115.

[30] E. P. Degarmo, J. T. Black, and R. A. Kohser, *Materials and Processes in Manufacturing 9th Ed.*, Wiley, USA, 2003.

[31] G. E. Dieter, *Mechanical Metalurgy*, McGraw-Hill, NY, USA, 1961.

[32] J. Dossett and G. E. Totten, *ASM Handbook, Volume 4A: Steel Heat Treating Fundamentals and Processes*, ASM International, OH United States, 2013.

[33] F. X. Dupé, J. M. Fadili, and J. L. Starck, *Linear inverse problems with various noise models and mixed regularizations*, ACM, 6 2012.

[34] P. Flenner, *Carbon Steel Handbook*, Electric Power Research Institute, California, USA, 2007.

[35] H. Friedberg, Stephen, J. Insel, Arnold, and E. Spence, Lawrence, *Linear Algebra 4th Ed.*, Prentice Hall, England, 2003.

[36] A. K. Galway and M. E. Brown, *Application of the arrhenius equation to solid state kinetics: Can this be justified?*, Thermochimica Acta, 386 (2002), pp. 91–98.

[37] J. P. Holman, *Heat Transfer 10th Ed.*, McGraw-Hill, NY, USA, 2010.

[38] J. M. Honig, *Thermodyamics 2nd Ed.*, Elsevier, USA, 1999.

[39] Inverse Problems, *Inverse problems: Systematic integration of data with models under uncertainty.* http://g2s3.com/labs/notebooks/inverseProblemPrototype.html, 2018. Accessed: 2021-05-15.

[40] ISO/IEC 17025:2017. *General requirements for the competence of testing and calibration laboratories.*, standard, Institute of Electronics and Computer, Switzerland, Nov. 2017.

[41] D. J. and T. G. E., *ASM Handbook, Volume 4: Heat Treating*, ASM International, OH, USA, 1991.

[42] J. Kaipio and E. Somersalo, *Statistical and Computational Inverse Problems*, Springer, USA, 2005.

[43] A. Kirsch, *An Introduction to the Mathematical Theory of Inverse Problems 2nd Ed.*, Springer, USA, 2011.

[44] E. M. Kutz, *Handbook of Environmental Degradation of Materials*, Elsevier, USA, 2018.

[45] K. J. Laidler, *The development of the arrhenius equation*, Journal of Chemical Education, 61 (1984), pp. 494–498.

[46] S. R. Logan, *The origin and status of the arrhenius equation*, Journal of Chemical Education, 59 (1982), pp. 279–281.

[47] M. R. Louthan, *Optical Metallography, ASM Handbook, Volume 10: Materials Characterizations*, ASM International, USA, 1986.

[48] W. G. Moffatt, G. W. Pearsall, and J. Wulff, *The Structure and Properties of Materials, Vol. I, Structure*, John Wiley & Sons, NY, USA, 1964.

[49] R. K. Nagle, E. B. Saff, and A. B. Snider, *Ecuaciones Diferenciales y Problemas con Valores en la Frontera*, Pearson Educación, México, 2004.

[50] A. S. Patnaik and J. L. Goldfarb, *Continuous activation energy representation*

*of the arrhenius equation for the pyrolysis of cellulosic materials: Feed corn stover and cocoa shell biomass*, Cellulose Chemistry and Technology, 50 (2015), pp. 311–320.

[51] M. Peleg, M. D. Normand, and M. G. Corradini, *The arrhenius equation revisited*, Critical Reviews in Food Science and Nutrition, 52 (2012), pp. 830–851.

[52] G. Petzow, *Metallographic Etching, 2nd Ed.*, ASM International, OH United States, 1999.

[53] T. Réti, M. Gergely, and P. Tardy, *Mathematical treatment of non-isothermal transformations*, Institute of Metals, 3 (1987), pp. 365–373.

[54] SAE J403 DEC2009. *Chemical compositions of SAE carbon steels*, standard, Society of Automotive Engineers, USA, Dec. 2009.

[55] P. Sebastiani, *A Tutorial on Probability Theory*, University of Massachusetts at Amherst, MA USA, 2008.

[56] A. K. Sinha, *Physical Metallurgy Handbook*, McGraw-Hill, New York, NY, 2003.

[57] R. E. Smallman and R. J. Bishop, *Modern Physical Metallurgy and Materials Enginnering, 6th ed.*, Butterworth Heinemann, Kent, UK, 1999.

[58] J. M. Smith, H. C. Van Ness, and M. M. Abbot, *Introduction to Chemical Engineering Thermodynamics 7th Ed.*, Mc Graw-Hill, USA, 2004.

[59] R. T. Smith and R. B. Minton, *Calculus 4th Ed.*, Mc Graw-Hill, NY, USA, 2012.

[60] M. Spivak, *Calculus 3rd Ed.*, Publish or Perish, Inc., Texas, USA, 1994.

[61] L. Suarez, R. Coto, X. V. Eynde, M. Lamberigts, and Y. Houbaert, *High temperature oxidation of ultra-low-carbon steel*, Defect and Diffusion Forum, 258-260 (2006), pp. 158–163.

[62] Thermodynamics, *Thermodynamics — Wikipedia, the free encyclopedia*. https://en.wikipedia.org/wiki/Thermodynamics, 2021. Accessed: 2021-05-15.

[63] G. F. Vander Voort, *Metallography Principles and Practice*, ASM International, New York, 1999.

[64] J. D. Verhoeven, *Steel Metallurgy for the Non-Metallurgist*, ASM International, New York, 2007.

[65] Wire Drawing, *Wire drawing — Wikipedia, the free encyclopedia*. https://en.wikipedia.org/wiki/Wire_drawing, 2021. Accessed: 2021-05-15.

[66] D. G. Zill, *Ecuaciones Diferenciales con Aplicaciones de Modelado 6a Ed.*, Thomson, México, 1997.

[67] M. Zorc, A. Nagode, J. Burja, B. Kosec, and B. Zorc, *Surface decarburization of the hypo-eutectoid carbon steel c45 during annealing in steady air at temperatures t ¿ ac1*, Metals, 8 (2018), pp. 425 – 450.